Petroleum Science 23 (2026) 3282–3298

Contents lists available at ScienceDirect

Petroleum Science

journal homepage: www.keaipublishing.com/en/journals/petroleum-science

Original Paper

Climate forcing of variations in sedimentary environments and organic matter accumulation in the Qingshankou Formation, Songliao Basin (NE China): Evidence from organic petrology and geochemistry

Zhao-Yang Wang [a,b], Jin-Qi Qiao [a,b,*], Qing-Yong Luo [a,b,**], Jia-Peng Wu [c], Man Lu [a,b], Ye Zhang [d,e], Mikhail Spasennykh [f], Hui-Long Lu [a,b], Lei He [a,b]

[a] Hainan Institute of China University of Petroleum (Beijing), Sanya, 572025, Hainan, China
[b] College of Geoscience, China University of Petroleum, Beijing, 102249, China
[c] China National Logging Corporation, Beijing, 100101, China
[d] National Joint Engineering Research Center for Shale Gas Exploration and Development, Chongqing Institute of Geology & Mineral Resources, Chongqing, 401120, China
[e] Key Laboratory of Shale Gas Exploration, Ministry of Natural Resources, Chongqing Institute of Geology & Mineral Resources, Chongqing, 401120, China
[f] Center for Petroleum Science and Engineering, Skolkovo Institute of Science and Technology, Moscow 121205, Russia

A R T I C L E I N F O

Article history:
Received 29 May 2025
Received in revised form 26 November 2025
Accepted 19 January 2026
Available online 23 January 2026

Edited by Min Li

Keywords:
Climatic driving
Organic matter accumulation
Sedimentary environment
Qingshankou Formation
Songliao Basin

A B S T R A C T

Lacustrine organic matter (OM) accumulation is a critical Earth's carbon sink and a source of hydrocarbon resources. The Upper Cretaceous Qingshankou Formation in the Songliao Basin archives an organic-rich sedimentation alongside paleoclimatic fluctuations, yet the mechanistic links between climate and OM enrichment remain unclear. Previous single-well studies are contentious and insufficient to unravel the complex, coupled sedimentary environmental feedbacks at the depression scale. This investigation integrates organic petrology and geochemical analyses of 24 core samples from the first (K_2qn^1) and second (K_2qn^2) members in the Central Depression, complemented by published data from 33 wells. Paleoclimate proxies reveal a climatic transition from the relatively humid K_2qn^1 interval to arid K_2qn^2 interval. This shift reconfigured the depositional system, altering terrestrial input, sedimentation rates, redox conditions, salinity, OM sources, and productivity. Crucially, it drove a fundamental OM accumulation change: high productivity in the relatively humid K_2qn^1 interval was offset by oxygenated waters conditions that limited preservation, whereas the arid K_2qn^2 interval, despite lower productivity, developed strong salinity stratification and benthic anoxia that dramatically enhanced OM preservation. Therefore, a climate-driven OM-preservation model for the study area was proposed, where aridity-controlled enhancement of water-column stratification and redox conditions dominated OM accumulation, overriding the productivity increases associated with relatively humid conditions. This model provides a new framework for understanding the formation of organic-rich lacustrine source rocks.

1. Introduction

Lakes, as pivotal components of the global carbon cycle, exhibit remarkable carbon sequestration efficiency, with modern lakes burying 0.2–1.6 Pg C/yr—up to eightfold faster than oceanic systems per unit area (Li et al., 2023). Notably, approximately 20% of atmospheric carbon emissions have been sequestered in lacustrine sediments through biogeochemical processes (Heathcote et al., 2015). Over geological timescales, organic-rich lacustrine sediments undergo diagenesis to form approximately 30% of global

* Corresponding author.
** Corresponding author.
E-mail addresses: jinqi.qiao@cup.edu.cn (J.-Q. Qiao), qingyong.luo@cup.edu.cn (Q.-Y. Luo).
Peer review under the responsibility of China University of Petroleum (Beijing).

https://doi.org/10.1016/j.petsci.2026.01.027
1995-8226/

hydrocarbon source rocks (Fryklund and Stark, 2020). In China, lacustrine successions host over 50% of proven hydrocarbon reserves (Zou et al., 2019). Beyond their economic importance, these organic-rich archives preserve high-resolution records of climate-ecosystem-sedimentation feedbacks (Li et al., 2023; Zhang et al., 2024).

The Late Cretaceous was a pivotal period of climatic transition from a super-hothouse to a cooling phase, characterized by widespread oceanic anoxic events, high sea levels, and large igneous province activity (Lei et al., 2022; Li et al., 2024; Scotese et al., 2021). Globally, this epoch witnessed extensive deposition of organic-rich mudstones in numerous sedimentary basins, including the Western Interior Seaway, the Atlantic (e.g., Maracaibo, Tarfaya, and Angola Basins), the Neo-Tethys (e.g., Tibetan Himalayas), and East Asian rift basins such as the Songliao Basin (Li et al., 2022; Zhang et al., 2024). The formation of these organic-rich units reflects complex feedbacks between climate-forced productivity, preservation conditions, and sedimentation rates (Sweere et al., 2016; Tyson, 2001). Paleoclimate changes regulated terrestrial input processes (e.g., weathering intensity and dilution) and key sedimentary parameters (e.g., salinity and benthic redox) by altering the precipitation-evaporation balance (Li et al., 2024; Qiao et al., 2023; Wu et al., 2023). These cascading effects ultimately governed surface biological productivity and the enrichment of organic matter (OM) (Lu et al., 2025; Wang et al., 2024).

The Songliao Basin, a premier continental archive of the Late Cretaceous in East Asia, hosts the organically-rich Qingshankou Formation (Fm.) (91.89–89.07 Ma), a major target for shale oil exploration and an ideal natural laboratory to investigate climate-lake interactions (Wang et al., 2016; Wu et al., 2023). The mechanism controlling OM accumulation in this formation, however, remains contentious, centered on two competing hypotheses. The productivity hypothesis attributes high total organic carbon (TOC) to algal blooms that outpaced microbial degradation. This scenario is linked to warm-humid climates, which enhanced precipitation and nutrient runoff, thereby stimulating primary productivity in the paleolake (Lu et al., 2025; Wu et al., 2023; Zhang et al., 2022). In contrast, the preservation hypothesis posits that anoxic bottom-water conditions were the dominant control on OM burial. Proponents argue that while warm-humid climates could lead to OM dilution and degradation, arid conditions promoted salinity-induced water-column stratification, creating a reducing benthic environment that drastically enhanced preservation efficiency (Li et al., 2024; Wang et al., 2023b; Xu et al., 2019). Although the influence of paleoclimate on sedimentary environments is acknowledged, it has often been treated as a peripheral triggering factor rather than the central control. In fact, paleoclimate serves as the critical bridge that translates astronomical forcing into diverse sedimentary responses, a connection evidenced by studies on astrochronology, lithofacies heterogeneity, and seawater incursion events in the basin (Chen et al., 2024; Tang et al., 2025; Wang et al., 2016). This climate-mediated control is manifested in pronounced heterogeneities across the Central Depression, including the debated vertical TOC variations between the K_2qn^1 and K_2qn^2 members and the uneven distribution of petroleum resources (Chen et al., 2024; Kang et al., 2024; Xu et al., 2019). These inconsistencies likely stem from the localized, single-well focus of prior studies, which cannot capture depression-scale dynamics (e.g., Li et al., 2024; Wu et al., 2023; Zhang et al., 2022). Therefore, a comprehensive depression-scale assessment integrating organic and inorganic geochemical data from multiple wells is essential. Such an approach is required to definitively establish how climatic transitions-controlled OM enrichment in the Qingshankou Fm., thereby refining predictive models for hydrocarbon exploration.

This investigation integrates organic petrographic, biomarker, and elemental geochemical approaches to decipher the mechanistic linkages between paleoclimatic forcing and the spatiotemporal evolution of OM-enriching sedimentary environments in the Qingshankou Fm. of the Central Depression. This study combines 24 core samples and thousands of published datasets from 35 wells, together with statistical analyses and correlation frameworks, to elucidate how climate changes modulated sedimentary environments and primary productivity, ultimately governing OM accumulation. The findings provide important insights into the genesis of high-quality source rocks in the Central Depression and into the broader climatic regulation of carbon cycling in lacustrine systems.

2. Geological setting

The Songliao Basin, a large-scale Mesozoic–Cenozoic hydrocarbon-bearing basin in NE China, contains a proven reserve of ~200 billion barrels of oil and 160 trillion cubic feet of natural gas (Fig. 1(a); Liu et al., 2023a; Zou et al., 2019). It is one of the global tier-one super basins as it meets the five key attributes of a super basin as defined by Fryklund and Stark (2020). The basin is divided into six tectonic units, including the Northern dip area, the Northeastern Uplift, the Western Slope, the Southeastern Uplift, the Southwestern Uplift, and the Central Depression which is the main hydrocarbon-producing region (Fig. 1(b)). A complete Jurassic–Neogene sedimentary succession is preserved, reaching a maximum thickness of 7,000 m in the depocenter (Zou et al., 2019). The most significant source rocks were deposited during the Upper Cretaceous Qingshankou Fm., which are subdivided into the K_2qn^1, K_2qn^2, and third member (Liu et al., 2023b). A progressive lacustrine regression from the K_2qn^1 to K_2qn^2 periods shaped the basin, during which extensive fluvial plains and delta fronts developed in the north, west, and south, whereas a narrow shore-shallow lacustrine belt surrounded a large, central deep lacustrine depocenter (Fig. 1(b); Feng et al., 2010; Zhu et al., 2017). It was within this central deep-lacustrine setting that the high-quality source rocks accumulated. A succession of high-quality source rocks exceeding 200 m occurs within the K_2qn^1 and the lower part of the K_2qn^2 intervals, constituting the most prospective target strata for petroleum exploration (Zou et al., 2019). Lithologically, these source rocks consist predominantly of grey to black mudstones and shales, interbedded with grey silty mudstones and minor siltstones (Fig. 2). Sedimentary structures, such as parallel lamination, rhythmic clay-siliciclastic laminae, and an absence of bioturbation, indicate deposition in a low-energy and anoxic environment (Sun et al., 2025). Mineralogically, the rocks are dominated by clay minerals, with subordinate quartz and plagioclase, and minor K-feldspar and calcite (Sun et al., 2025). The combination of the fine-grained lithology, organic-rich composition, and anoxic sedimentary environment makes these strata an ideal subject for investigating OM accumulation.

The tectonic evolution of the Songliao Basin progressed through four stages: rifting (Jurassic–Early Cretaceous), thermal subsidence (Late Cretaceous), structural inversion (Late Cretaceous–Paleogene), and contraction (Neogene–Quaternary) which governed stratigraphic distribution and depositional features of the Qingshankou Fm. in the Central Depression (Feng et al., 2010; Zou et al., 2019). During the rifting stage, fault-controlled lacustrine basins developed, establishing the spatial framework and sedimentary material for the deposition of the Qingshankou Fm. in the Central Depression. Subsequently, the thermal subsidence stage fostered semi-deep to deep lacustrine environments. This period was punctuated by intermittent marine incursions, which may have enhanced preservation via salinity stratification but also perturbed freshwater ecosystems through abrupt salinity fluctuations (Chen et al., 2024; Wu et al., 2023; Xu et al., 2021). The

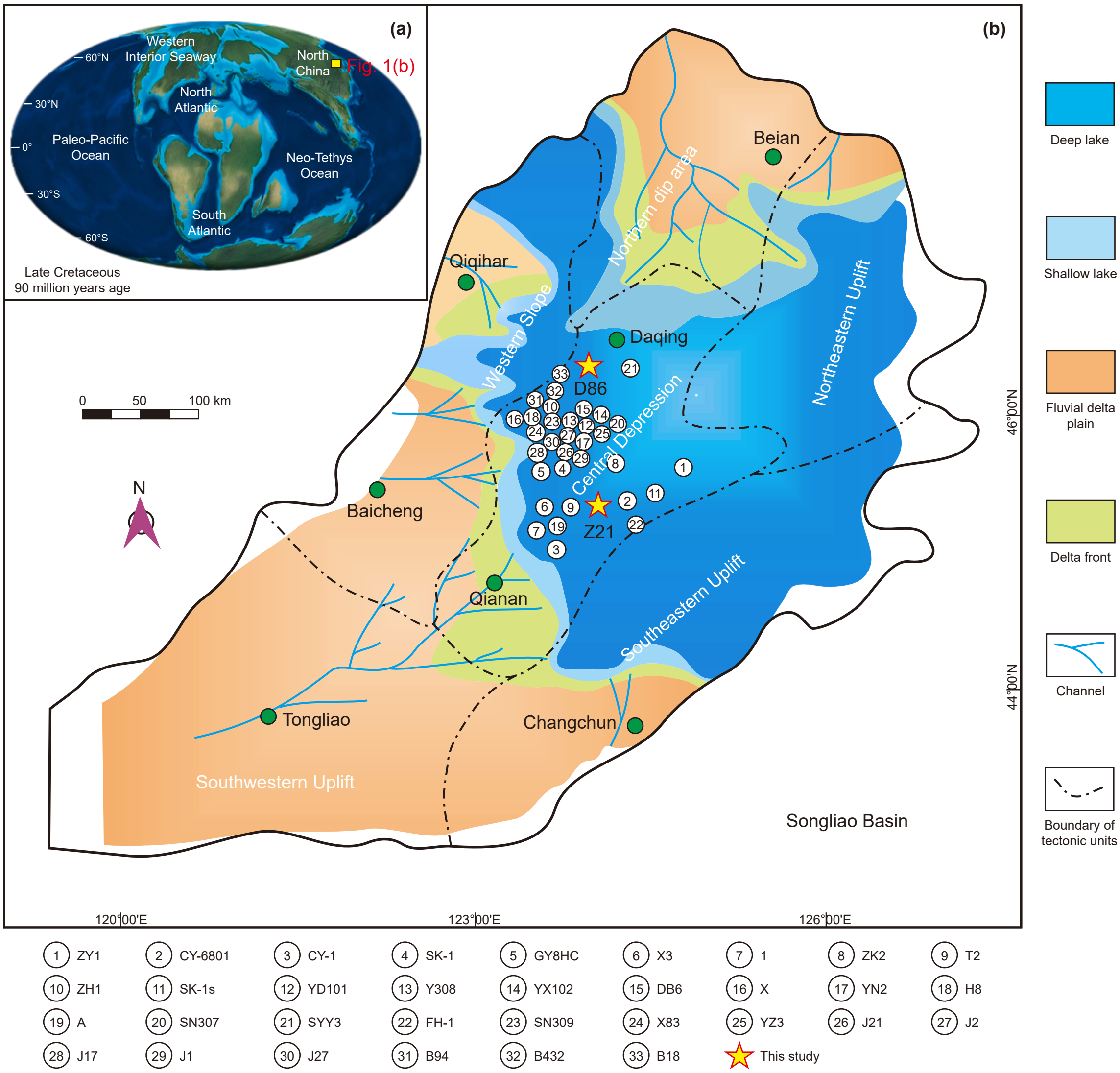

Fig. 1. **(a)** Location of the Songliao Basin during the Late Cretaceous, **(b)** six sub-tectonic units, sedimentary facies map of Member 1 (modified from Wu et al. (2023)), and investigated 33 wells of Qingshankou Fm. Note: the numbers in the circles represent wells in literature.

subsequent structural inversion stage uplifted and compressed the basin, facilitating the entry of source rocks into the early oil window, while tectonic stability during the contraction stage favored the preservation of OM (Feng et al., 2010; Li et al., 2024).

3. Materials and methods

3.1. Samples and preparation

A total of 24 mudstone core samples were collected from wells D86 and Z21, and thousands of published data were compiled from 33 wells in the Central Depression (Figs. 1(b) and 2). Each core sample was split into two aliquots: one was prepared as a polished, epoxy-embedded block (2 cm diameter) for organic petrography, and the other was finely ground (80–120 mesh) for subsequent geochemical analyses.

3.2. Organic petrology

Maceral composition was analyzed using a Leica DM4500P microscope equipped with a 50× oil-immersion objective. The proportions of vitrinite, inertinite, and minerals were quantified by point counting under reflected white light, while the mineral-bituminous groundmass and lamalginite were point-counted under fluorescent light. Vitrinite reflectance (R_o) was measured using an MPV-SP microscope photometer calibrated with a yttrium aluminum garnet standard (0.889%). Over 50 measurement points were obtained for each sample and averaged using Fossil software. A detailed description of this methodology follows Qiao et al. (2024).

3.3. Organic geochemistry

3.3.1. Conventional organic geochemistry

TOC and total sulfur (TS) contents were determined using a LECO-CS230 Analyzer. Prior to analysis, samples were acid-treated with dilute HCl to remove inorganic carbon, then repeatedly rinsed with deionized water until neutral (pH~7). Rock-Eval pyrolysis was performed on 50 mg of samples using an OGE-II instrument, yielding data for free hydrocarbons (S_1), pyrolysis hydrocarbons (S_2), and temperature of the maximum pyrolysis yield (T_{max}). The analytical procedures described above were detailed by Qiao et al. (2024).

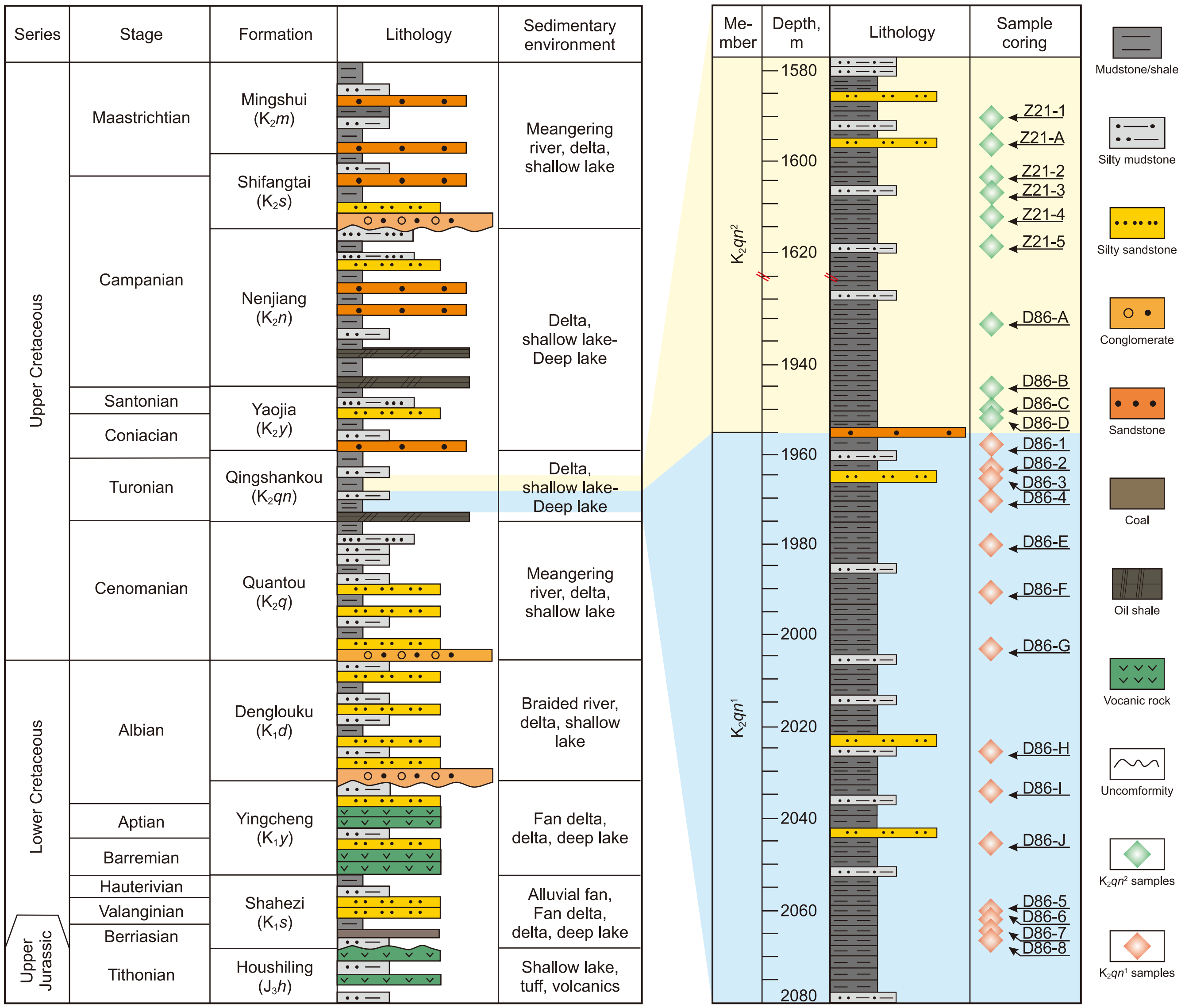

Fig. 2. The comprehensive column showing lithology (modified from Wu et al. (2023)) and sampling locations.

3.3.2. Molecular organic geochemistry

Extractable OM (EOM) was extracted from 80 g of samples using a 500 mL Soxhlet extractor and was subsequently separated into asphaltenes (Asp), saturated hydrocarbons (Sat), aromatic hydrocarbons (Aro), and non-hydrocarbons (Non) by silica gel and alumina column chromatography. The aliphatic and aromatic fractions were analyzed using Agilent 6890-5975i and Agilent 7890B-5977A GC-MS systems, respectively. Analytical conditions follow in Qiao et al. (2024).

The following compounds were identified by their characteristic mass fragments (*m/z*): *n*-alkanes series, isoprenoids (pristane and phytane (Pr and Ph, *m/z* 85), C_{25} isoprenoid and C_{30} isoprenoid (PMI and squalene, *m/z* 183)), and β-carotane (*m/z* 125); terpenoids containing tricyclic terpane series, C_{24} tetracyclic terpane, hopanes series, gammacerane (TTs, C_{24}TeT, H, and Gamm, *m/z* 191), and methylhopanoids series (MeH, *m/z* 205); regular steranes series and C_{30} 4-desmethylsteranes (RS and C_{30} 4-DMRS, *m/z* 217); aryl isoprenoids series (*m/z* 133); methyltrimethyltridecylchromans (MTTCs, δ-MTTC (*m/z* 121), $\beta/\zeta/\gamma$-MTTC isomeric forms (*m/z* 135), and α-MTTC (*m/z* 149)); fluorene-series compounds (fluorene (F, *m/z* 166), dibenzofuran (DBF, *m/z* 168), dibenzothiophene (DBT, *m/z* 184)); naphthalene derivatives (trimethylnaphthalene (TMN, *m/z* 170), tetramethylnaphthalene (TeMN, *m/z* 184)); phenanthrene-series polycyclic aromatic hydrocarbons (PAHs, phenanthrene (PHE, *m/z* 178), methylphenanthrene (MP, *m/z* 192), dimethylphenanthrene (DMP, *m/z* 206)); higher plant inputs polycyclic aromatic hydrocarbons (cadalene (*m/z* 183), iso-hexamethylnaphthalene (*i*-HMN, *m/z* 197), retene (*m/z* 219)); and triaromatic steranes series (TAS, *m/z* 231).

3.4. Elemental geochemistry

The concentrations of major, trace, and rare earth elements were determined using an inductively coupled plasma optical emission spectrometry (ICP-OES) with an Agilent 720 spectrometer and inductively coupled plasma mass spectrometry (ICP-MS) with a PlasmaQuant MS analytical system, respectively. Detailed experimental conditions and procedures refer to Qiao et al. (2025). The index of compositional variability (ICV), weathering index of Parker (WIP), chemical index of alteration (CIA), plagioclase index of alteration (PIA), enrichment factor (EF), and biogenic elements (X_{bio}) were calculated, as summarized in Table S1.

3.5. Statistical methodology

The selected dataset's normality was assessed using the Shapiro-Wilk method. Pearson's correlation (r) analysis was applied to quantify linear associations between variables in normally distributed datasets, and Spearman's rank-order correlation (ρ) was employed for non-normally distributed data (Wang et al., 2023a). Statistical significance thresholds for the normality test and correlation strength evaluation were uniformly set at 0.05.

4. Results

4.1. Basic geochemical characteristics

The TOC contents of the studied samples range from 0.85% to 4.64%, with the K_2qn^1 intervals averaging 2.06%, which is lower than the average value of 2.99% in the K_2qn^2 intervals (Table S2). Consistent with the TOC results, the $S_1 + S_2$ and EOM contents are lower in the K_2qn^1 interval than in the K_2qn^2 interval (Table S2). The hydrogen index (HI) values exhibit a uniform kerogen type (Table S2). The T_{max} values of K_2qn^1 and K_2qn^2 samples range from 437 to 451 °C and 433–447 °C, respectively (Table S2). Moreover, the EOM is dominated by Sat + Aro proportion (avg. 73.79%) with a low polar proportion (Non + Asp: avg. 26.21%) (Table S2).

4.2. Maceral composition and vitrinite reflectance

The maceral composition of the studied samples is dominated by lamalginite and mineral-bituminous groundmass, both exhibiting bright yellow to yellowish-green fluorescence (Fig. 3(b), (d), (e), (g), and (i)). In contrast, vitrinite and inertinite are subordinate, comprising only 5%–10% of the total maceral volume. Prasinophyte green algae are abundant in the K_2qn^2 samples (Fig. 3(e)) with minor amounts of funginite (Fig. 3(h)). The R_o values of all studied samples exhibit only minor differences, with average values of 0.74% and 0.72%, respectively (Table S2). Pyrite is ubiquitous, occurring as either euhedral crystals or framboidal aggregates (diameters generally <10 μm) (Fig. 3).

4.3. Biomarkers

4.3.1. Aliphatic hydrocarbons

The n-alkane distributions of the K_2qn^1 samples are dominated by short-chain ($\leq n$-C_{20}) component (n-C_{max} = n-C_{20}; Fig. 4(a)), while K_2qn^2 samples are characterized by elevated abundances of intermediate (n-C_{21-25}) and long-chain ($\geq n$-C_{26}) components (n-C_{max} = n-C_{23}; Fig. 4(b)). The $\sum n$-C_{21-}/$\sum n$-C_{22+} ratios are higher in the K_2qn^1 samples, ranging from 0.41 to 1.18 (avg. 0.84), compared to the K_2qn^2 samples (0.42–0.85, avg. 0.66; Table S3). The terrestrial/aquatic ratio (TAR) values of K_2qn^1 samples (0.35–1.44; avg. 0.61) are lower than those in the K_2qn^2 samples (0.51–1.23, avg. 0.79). Similarly, the other geochemical parameters, including Pr/Ph, Pr/n-C_{17}, Ph/n-C_{18}, PMI/n-C_{max}, β-carotane/n-C_{max}, (C_{19} + C_{20})/(C_{23} + C_{24})TT, C_{24}TeT/(C_{24}TeT + C_{23}TT), Gamm/C_{30}H, 2α-MeH/C_{30}H, and 3β-MeH/C_{30}H ratios, reveal significant differences in the two intervals (Fig. 4(c) and (d); Table S3). Besides, this divergent pattern is evident in the proportion of regular steranes (C_{29}RS ≈ C_{27}RS > C_{28}RS and C_{29}RS > C_{28}RS > C_{27}RS) and in the C_{30} 4-DMRS/$\sum C_{27-29}$RS ratio (avg. 0.19 and 0.23; Fig. 4(e) and (f)). Hopane parameters show a slight difference between the two sub-member samples, including Ts/(Ts + Tm) of 0.54–0.79 (avg. 0.67) for the K_2qn^1 samples and of 0.39–0.73 (avg. 0.60) for the K_2qn^2 samples as well as C_{29}Ts/(C_{29}Ts + C_{29}H) ratios of 0.51–0.71 (avg. 0.63) for the K_2qn^1 samples and of 0.41–0.57 (avg. 0.48) for the K_2qn^2 samples (Table S3). Furthermore, the C_{31}H 22S/(22S + 22R) and C_{32}H 22S/(22S + 22R) ratios show consistent results (Table S3).

4.3.2. Aromatic hydrocarbons

The aromatic hydrocarbons are characterized by abundant phenanthrene-series PAHs, naphthalene derivatives, and triaromatic steroids (Fig. 5(a)–(b)). These molecular indices, trimethylnaphthalene ratio (TMNr), tetramethylnaphthalene ratio (TeMNr), methylphenanthrene index-1 (MPI-1), and the C_{28}TAS 20S/(20S + 20R) stereoisomeric ratio, show similar ranges and average values (Table S4). However, OM source indices, including log (1-MP/9-MP), log (1,7-DMP/(1,3- + 3,9- + 2,10- + 3,10-DMP)), log ((1,2,7 + 1,6,7-TMN)/1,3,7-TMN), and log (1,2,5-TMN/1,3,6-TMN), demonstrate significant differences between the two studied intervals (Table S4). Similarly, ranges and average values of the higher plant index (HPI) and higher plant parameter (HHP) exhibit remarkably lower values in the K_2qn^1 samples compared to those in the K_2qn^2 samples (Table S4). Among the fluorene-series compounds, DBT exhibits the highest relative abundance (43.57%–93.67%, avg. 67.53%), followed by DBF (0.64%–39.53%, avg. 17.30%) and F (2.25%–31.07%, avg. 15.17%; Fig. 5(a) and (b)). MTTC series are 0.05–0.39 (avg. 0.25) in the K_2qn^1 samples and 0.03–0.21 (avg. 0.12) in the K_2qn^2 samples. Similarly, a pronounced difference is observed in the aryl isoprenoid ratio (AIR), which is higher in the K_2qn^1 samples compared to the K_2qn^2 samples (Table S4).

4.4. Major, trace elements, and rare earth elements

No significant differences were observed among the studied samples in elemental proxies for sediment hydraulic sorting, recycling, and provenance, including ICV (1.08–6.42; except for sample Z21-1), Eu_{anom} (0.55–0.80), Al/Si (0.13–0.45), Th/Sc (0.57–1.30), Zr/Sc (9.97–20.26), La/Th (1.88–4.11), Hf concentration (1.42–5.48 ppm), La/Sc (1.38–4.70), and Co/Th (0.90–1.73) ratios (Tables S1 and S5). In contrast, paleoclimate-sensitive elements show differences between the two studied intervals. The K_2qn^1 interval exhibits slightly lower average WIP (52.20), $CIA_{-corrected}$ (71.20), PIA (71.75), C_{-value} (0.53), and Rb/Sr (0.26) compared with those of the K_2qn^2 interval, which are 51.29, 68.68, 69.01, 0.38, and 0.15, respectively (Tables S1 and S5). The detrital input parameters Ti/Al (10^{-4}), Zr/Al (10^{-4}), and Si/Al ratios in the K_2qn^1 samples are 243.03–581.85 (avg. 377.64), 17.35–27.89 (avg. 19.59), and 2.99–7.60 (avg. 3.73), respectively, which are similar to those of the K_2qn^2 samples (176.04–467.14 (avg. 423.83), 17.28–22.20 (avg. 20.92), and 2.21–4.78 (avg. 3.33), respectively (Table S5)). Redox-sensitive proxies in the K_2qn^1 samples, including Mo_{EF} (0.81–8.19, avg. 3.43), U_{EF} (0.96–2.05, avg. 1.43), and C_{org}/P (13.57–151.44, avg. 70.71), exhibit reduced values compared to those in the K_2qn^2 samples (Mo_{EF}: 2.31–7.03, avg. 5.27; U_{EF}: 1.42–2.44, avg. 1.85; C_{org}/P: 87.59–546.87, avg. 175.71). Paleosalinity proxies Sr/Ba show an increasing trend from the K_2qn^1 interval (0.22–1.88, avg. 0.90) to the K_2qn^2 interval (1.03–3.04, avg. 1.71; Table S5). Differences also in productivity proxies between the two intervals are indicated by the Ba_{bio}, Ba_{bio}/Al (10^{-4}), P/Al (10^{-4}), Cu/Al (10^{-4}), Cu/Ti, and Ni/Al (10^{-4}) ratios (Tables S1 and 5).

5. Discussion

5.1. Reliability of parameters

5.1.1. Thermal maturity

Thermal maturity of OM constrains both hydrocarbon generation potential and the reliability of biomarker interpretations (Peters et al., 2005). The combined T_{max} and R_o values indicate that

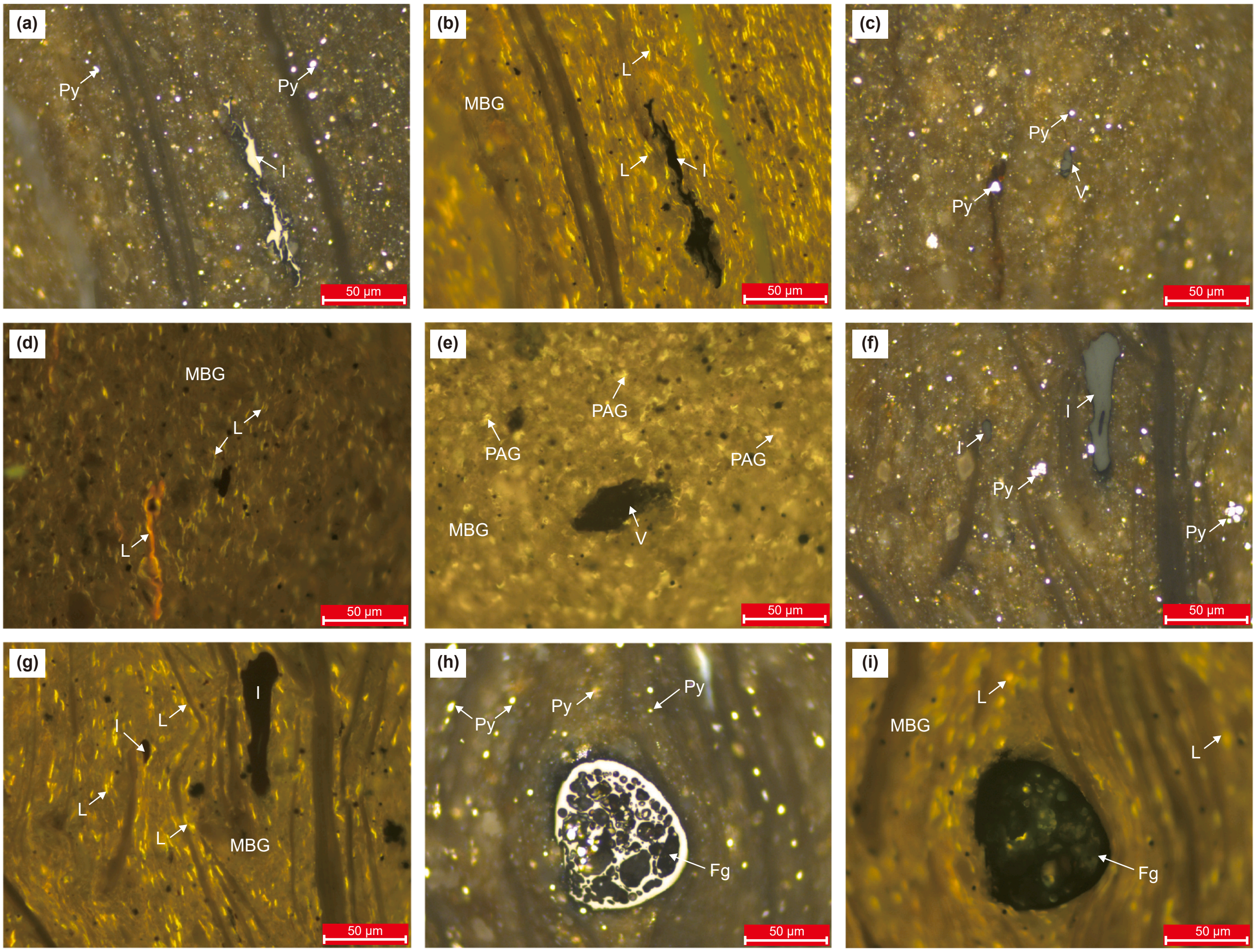

Fig. 3. Microphotographs of macerals in the Qingshankou Fm. source rocks under reflected light ((**a**), (**c**), (**f**), (**h**)) and under fluorescent light ((**b**), (**d**), (**e**), (**g**), (**i**)). Samples (**a**)–(**b**) D86-1 and (**c**)–(**d**) D86-5 from the K_2qn^1 interval; Samples (**e**) Z21-2, (**f**)–(**g**) Z21-3, and (**h**)–(**i**) Z21-5 from the K_2qn^2 interval. Note, L-lamalginite, MBG-mineral-bituminous groundmass, V-vitrinite, I-inertinite, Fg-Funginite, PAG-prasinophyte green algae, and Py-pyrite.

the OM in the most studied samples are within early to peak oil generation stage (Fig. 6(a)). Thermal maturity-related sterane and hopane ratios in this study and the published datasets, as well as by aromatic hydrocarbon indices (e.g., C_{28}TAS 20S/(20S + 20R) and MPI-1; Table S4), show consistent results (Fig. 6(b) and (c)). However, certain maturity parameters, such as Ts/(Ts + Tm) and C_{29}Ts/(C_{29}Ts + C_{29}H) ratios, can be affected by clay catalysis and high-salinity conditions, resulting in greater variability (Fig. 6(d)) (Peters et al., 2005; Seifert and Moldowan, 1978). Therefore, the similar thermal maturity of the two sub-members ensures that observed differences in biomarker signatures primarily reflect variations in OM source and depositional conditions, rather than thermal maturity effects.

5.1.2. Provenance and sorting

To ensure the reliable interpretation of paleoclimate proxies, potential overprints from sediment recycling, compositional variations, and hydraulic sorting are evaluated and excluded. The cross-plot of Th/Sc vs. Zr/Sc indicates that the samples predominantly are the first-cycle sedimentation (Fig. S1(a); McLennan, 1989), which is supported by the absence of quartz enrichment (Fig. S2(a); Garzanti et al., 2013). The compositional immaturity of the studied samples is confirmed by the ICV > 1 (Cox et al., 1995; Table S1). The plots of La/Th vs. Hf, La/Sc vs. Co/Th, and Th/Sc vs. Eu_{anom} reveal that the majority of the samples are felsic-dominated provenance (Fig. S1(b)–(d); Floyd and Leveridge, 1987). Critically, the Al/Si ratio, assessing hydraulic sorting intensity (Qiao et al., 2023), shows no significant correlation with both WIP and CIA (Fig. S2(b) and (c)), and samples plot near the compositional origin in a Zr-enrichment diagram (Fig. S2(d)). These consistent lines of evidence indicate the studied samples are unaffected by the sediment recycling, provenance variation, and hydraulic sorting, ensuring that the geochemical signatures can be attributed to primary paleoclimatic conditions.

5.2. Paleoclimate

Multiple geochemical proxies document a pronounced paleoclimatic shift from relatively warm/humid conditions in the K_2qn^1 interval to arid/cold conditions with limited chemical weathering in the K_2qn^2 interval. This trend is evident in Ga/Rb vs. K_2O/Al_2O_3 ratios (Roy and Roser, 2013; Wang et al., 2023b) and is corroborated by major element relationships (SiO_2 vs. $Al_2O_3 + K_2O + Na_2O$; Suttner and Dutta, 1986) (Fig. 7(a) and (b)). Furthermore, following established classification schemes (Fedo et al., 1995), the K_2qn^1 samples exhibit moderately elevated $CIA_{\text{-corrected}}$ values (>70), consistent with moderate chemical weathering under persistent relatively

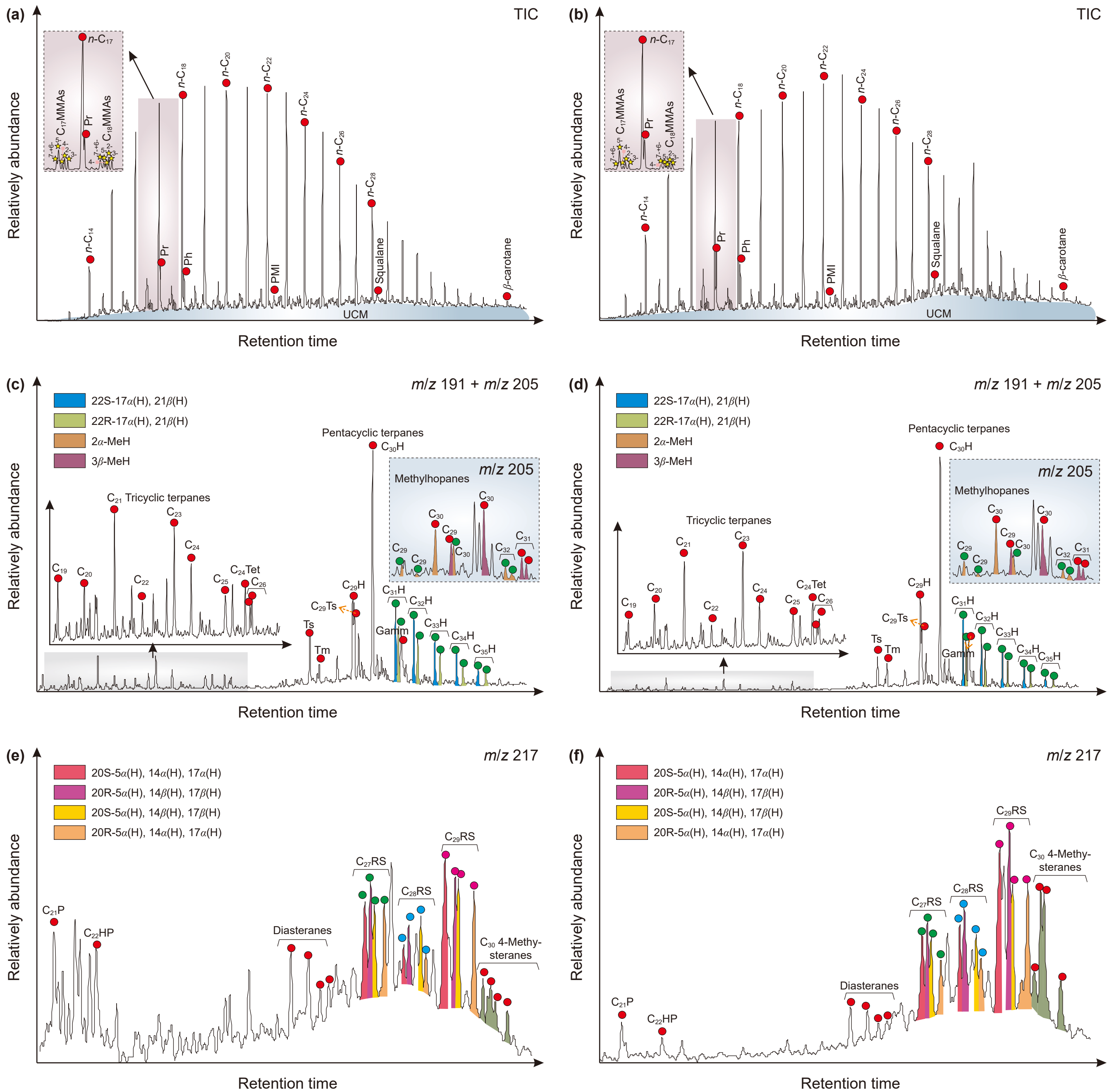

Fig. 4. The partial mass chromatograms of aliphatic hydrocarbons in the Qingshankou Fm. source rocks (figures on the left represent sample D86-1 from the K_2qn^1 interval, and on the right represent sample Z21-2 from the K_2qn^2 interval). Mass chromatograms showing **(a)**–**(b)** the distribution of *n*-alkanes series, isoprenoids, and β-carotane; **(c)**–**(d)** terpanes (*m/z* 191) and methylhopanoids (*m/z* 205); and **(e)**–**(f)** steranes (*m/z* 217).

humid conditions (Fig. 7(c)). In contrast, $CIA_{\text{-corrected}}$ values of the K_2qn^2 samples approach 70, suggesting a climatic transition toward arid conditions (Fig. 7(d)). This climatic fluctuation is further supported by the changes in PIA values (Fig. 8(a)) and Rb/Sr ratios in the studied samples (Figs. 7(d) and 8(b); Wang et al., 2024; Liu et al., 2022). Similar results can be observed from the $C_{\text{-value}}$ (Figs. 7(d) and 8(c); Wang et al., 2024) and Sr/Cu ratios (Fig. 7(d); Chen et al., 2024). Conclusively, a climatic transition was suggested to occur from the relatively humid conditions in the K_2qn^1 interval to distinctly more arid conditions in the K_2qn^2 interval.

Palynological evidence provides independent verification of this climatic zonation. The K_2qn^1 interval preserves a spore-pollen assemblage dominated by Fern Spore, accompanied by gymnosperm taxa, reflecting mixed coniferous-broadleaf vegetation characteristic of relatively humid ecosystems (Zhao et al., 2014). Conversely, the K_2qn^2 interval is distinguished by proliferating xerophytic spores and drought-tolerant gymnosperm, recording a climatic shift toward semi-arid conditions (Zhao et al., 2014). This trend toward aridity is further corroborated by coupled positive excursions in inorganic $\delta^{13}C$ and $\delta^{18}O$ values, consistent with enhanced evaporation and a more hydrologically closed lake system during K_2qn^2 deposition (Jones et al., 2018; Zhang et al., 2024). This regional climatic trend coincided with a global decline in deep-ocean temperatures, highlighting a broader cooling phase (Friedrich et al.,

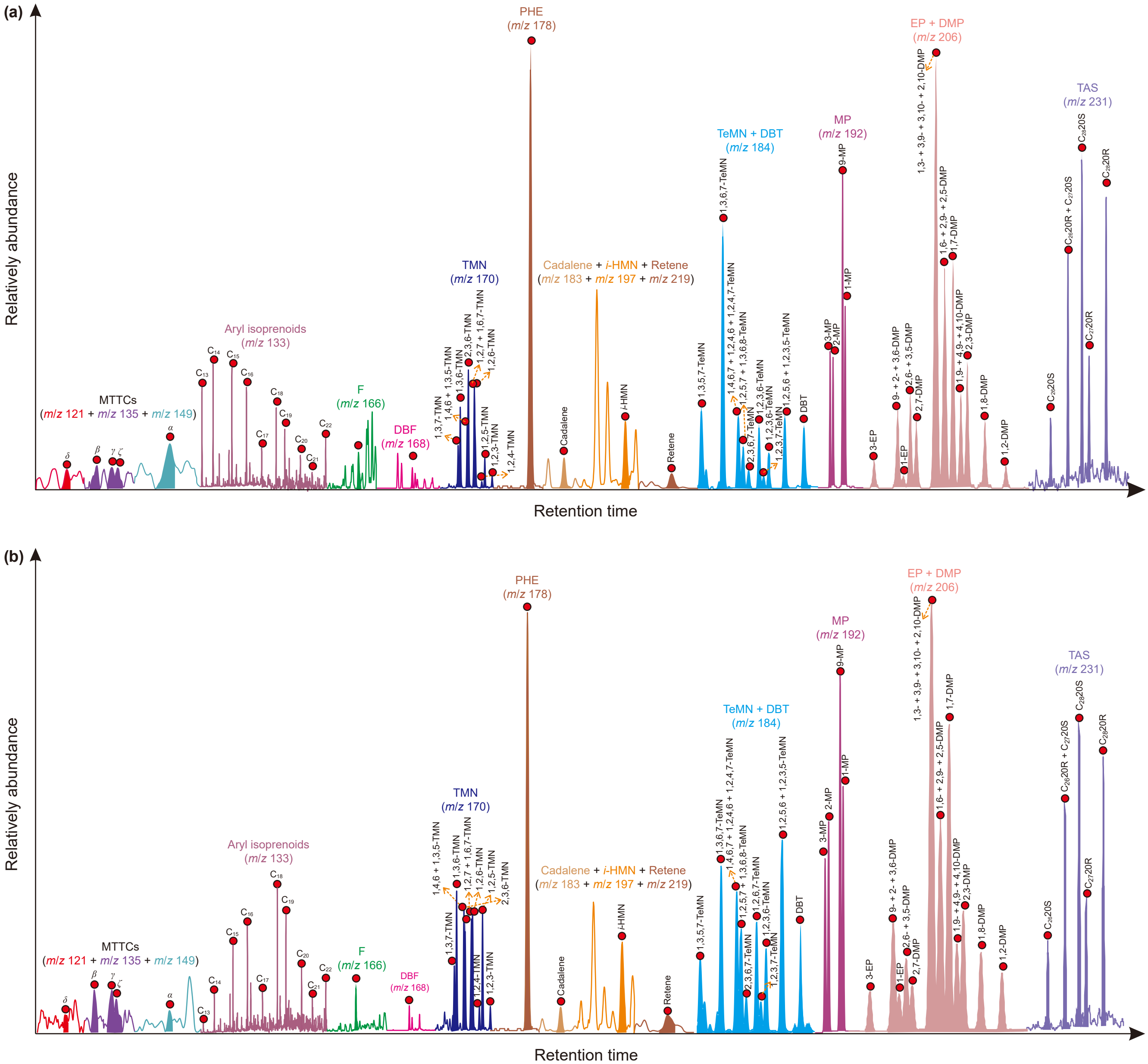

Fig. 5. The mass chromatograms of aromatic hydrocarbons in the Qingshankou Fm. source rocks. Samples **(a)** D86-1 and **(b)** Z21-2 from the K_2qn^1 and K_2qn^2 intervals, respectively.

2012). While occurring within the overarching Cretaceous greenhouse climate, high-resolution records reveal superposition of short-term aridity events during deposition of the Qingshankou Fm. (Li et al., 2024; Wu et al., 2023; Zhang et al., 2022). The onset of this cooling and aridification trend was likely driven by combined forcings, including volcanogenic aerosol effects on radiation budgets, orbital modulation of insolation, and perturbations to the global carbon cycle affecting atmospheric CO_2 levels (Lu et al., 2025; Zhang et al., 2024). In summary, an unequivocal climatic shift occurred from the relatively humid conditions of the K_2qn^1 interval to the sustained arid climate that prevailed during the K_2qn^2 interval.

5.3. Sedimentary environment

5.3.1. Terrestrial input and sedimentation rate

Elemental ratios serve as effective proxies for detrital input, with Al (primarily from clay minerals) representing fine-grained components, and Ti, Zr, and Si associated with heavy or coarse-grained minerals (Tribovillard et al., 2006). As shown in Fig. 8(d), the consistently low variability in Ti/Al (10^{-4}) ratios indicates stable terrigenous input and transport distances throughout the studied intervals, despite climatic cooling and weakened weathering. This interpretation is supported by minimal fluctuations in

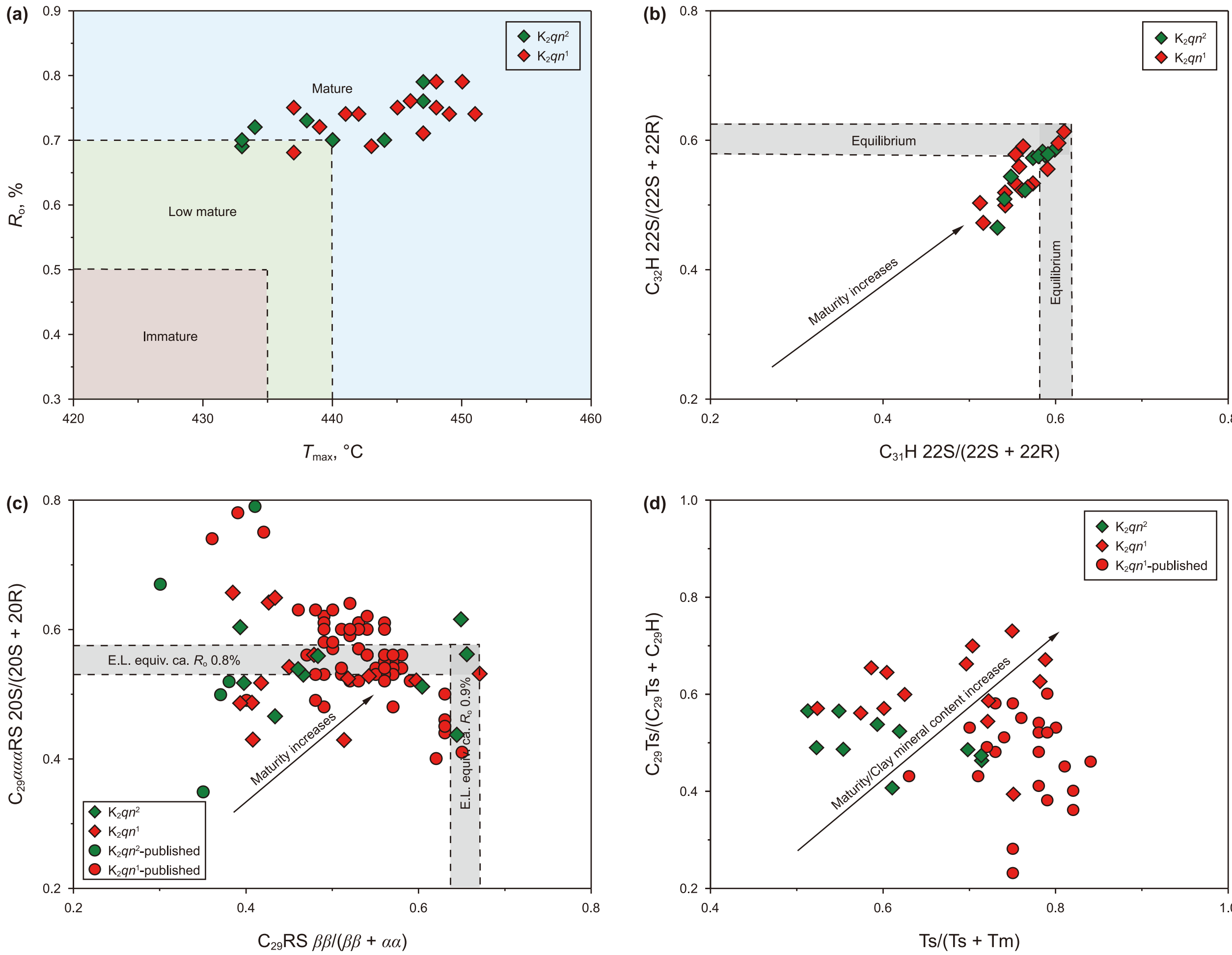

Fig. 6. Thermal maturity indicators for the Qingshankou Fm. source rock. Cross-plots of **(a)** T_{max} vs. R_o, **(b)** Ts/(Ts + Tm) vs. C_{29}Ts/(C_{29}Ts + C_{29}H), **(c)** C_{31}H 22S/(22S + 22R) vs. C_{32}H 22S/(22S + 22R), and **(d)** C_{29} $\alpha\alpha\alpha$ 20S/(20S + 20R) vs. C_{29} $\beta\beta/(\beta\beta + \alpha\alpha)$. Here, E.L. equiv. ca. represents the isomerization equilibrium level equivalent to the R_o value.

Zr/Al and Si/Al ratios (Fig. 8(e)) and aligns with regional records of steady clastic flux (Jones et al., 2018; Wu et al., 2023; Li et al., 2024; Tang et al., 2025). Although humid-to-arid transitions typically suppressed clastic fluxes due to enhanced evaporation and reduced hydrodynamic energy (Qiao et al., 2023), the stability during the K_2qn^2 interval may be attributed to a compensating mechanism. Reduced temperature and precipitation diminished vegetation cover, weakening soil cohesion and enhancing surface erodibility (Lu et al., 2025). The resulting increase in erosional potential likely offset the decline in sediment transport capacity, maintaining a near-steady detrital flux.

Sedimentation rate analyses, however, reveal a clear climatic response: rates shifted from higher in the K_2qn^1 interval to lower in K_2qn^2 interval (Figs. 8(f) and S3(c)). This suggests that the primary control on sedimentation evolved from efficient transport under more humid conditions (K_2qn^1 interval) to hydrodynamic limitation under arid conditions (K_2qn^2 interval). Thus, while increased erosional supply countered reduced transport capacity to stabilize detrital flux, the net accumulation rate still declined. Furthermore, this climate-driven transition likely operated in conjunction with broader factors, including tectonic subsidence, astronomical forcing, and biogenic processes (Ding et al., 2015).

5.3.2. Paleoredox

The paleoredox conditions were reconstructed using coupled C-S-Fe systematics (DOP_T, TOC-S-Fe) (Algeo and Liu, 2020; Dean and Arthur, 1989). A synthesis of published datasets indicates that most samples from the relatively humid K_2qn^1 interval plot within the oxic field, whereas those from the arid K_2qn^2 interval cluster within the oxic-dysoxic transition zone (Figs. 8(g) and 9(a)). The detection of aryl isoprenoids, derived from the cleavage of isorenieratene and β-isorenieratene (specific to anaerobic photosynthetic green sulfur bacteria), provides evidence for photic zone euxinia (PZE; Peters et al., 2005; Zheng et al., 2022b). Concurrently, a progressive decrease in the aryl isoprenoid ratio across the transition (Fig. 5(a) and (b); Table S4) signals an expansion and intensification of water-column hypoxia, driven by enhanced evaporation and hydrological closure under arid conditions.

Multiple redox-sensitive proxies (Mo, U, P, and framboidal pyrite) are common proxies for assessing oxygenation states (Algeo and Liu, 2020; Tribovillard et al., 2012). Most studied samples plotting near the suboxic to weakly anoxic boundary defined by Tribovillard et al. (2012) (Fig. 9(d)) and the widespread occurrence of framboidal pyrites with sizes of predominantly <10 μm (Fig. 3) support reducing conditions in the bottom waters. Notably, Mo_{EF}, U_{EF}, and C_{org}/P ratios are relatively lower in the K_2qn^1 interval compared to the K_2qn^2 interval, which have been consistently observed across multiple datasets (Figs. 9(d) and S3(d)). The marked transition from relatively humid (K_2qn^1 interval) to arid (K_2qn^2 interval) conditions perturbed the hydrological equilibrium, led to lake contraction, enhanced water-column

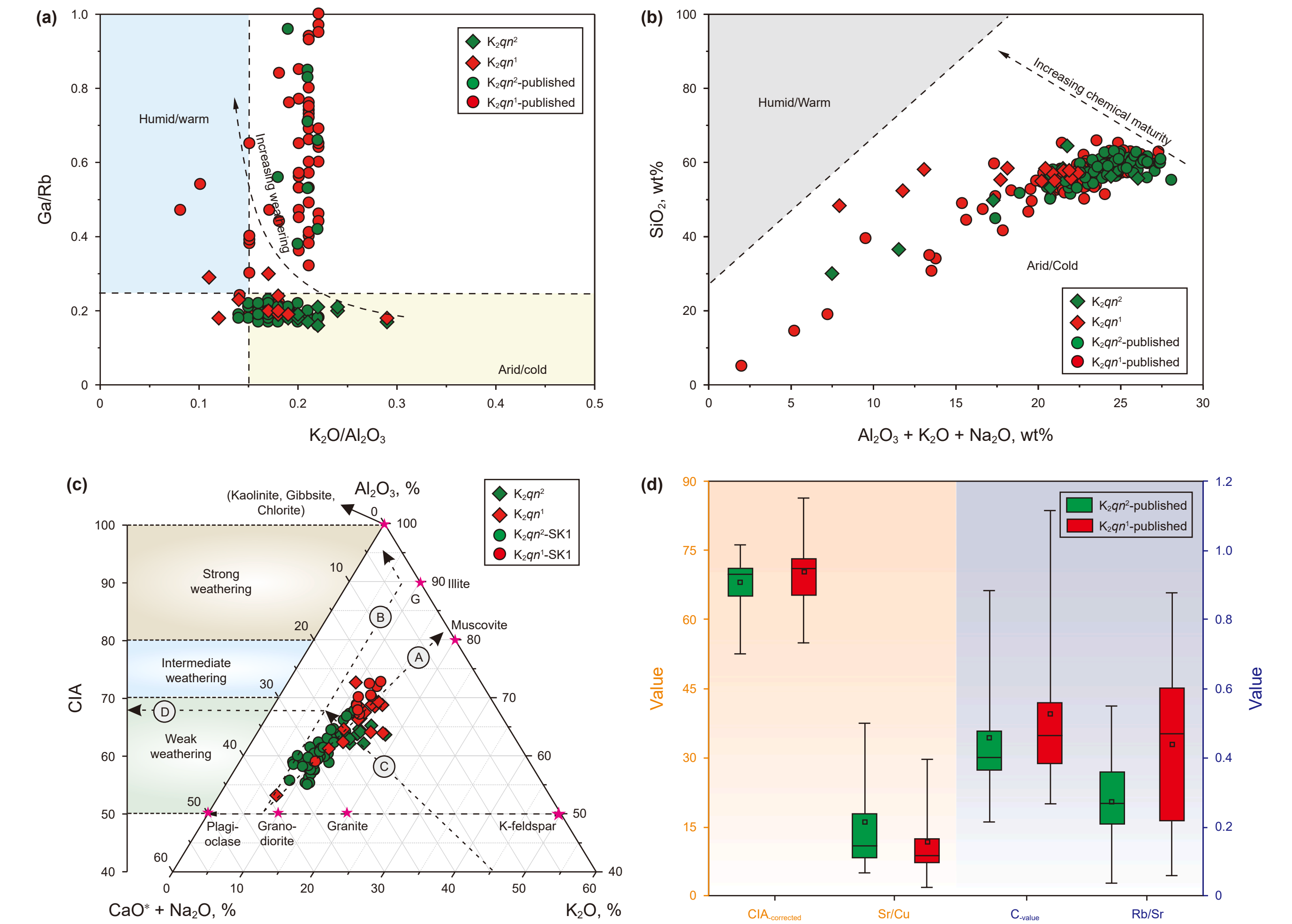

Fig. 7. (a) Cross-plot of Ga/Rb vs. K_2O/Al_2O_3 (after Qiao et al., 2022), **(b)** $Al_2O_3 + K_2O + Na_2O$ vs. SiO_2 (Suttner and Dutta, 1986), **(c)** Al_2O_3-K_2O-($CaO^* + Na_2O$) ternary diagram (Fedo et al., 1995; Well SK-1 date from Jones et al. (2018)), and **(d)** box plot of published data indicating paleoclimatic changes and the degree of chemical weathering.

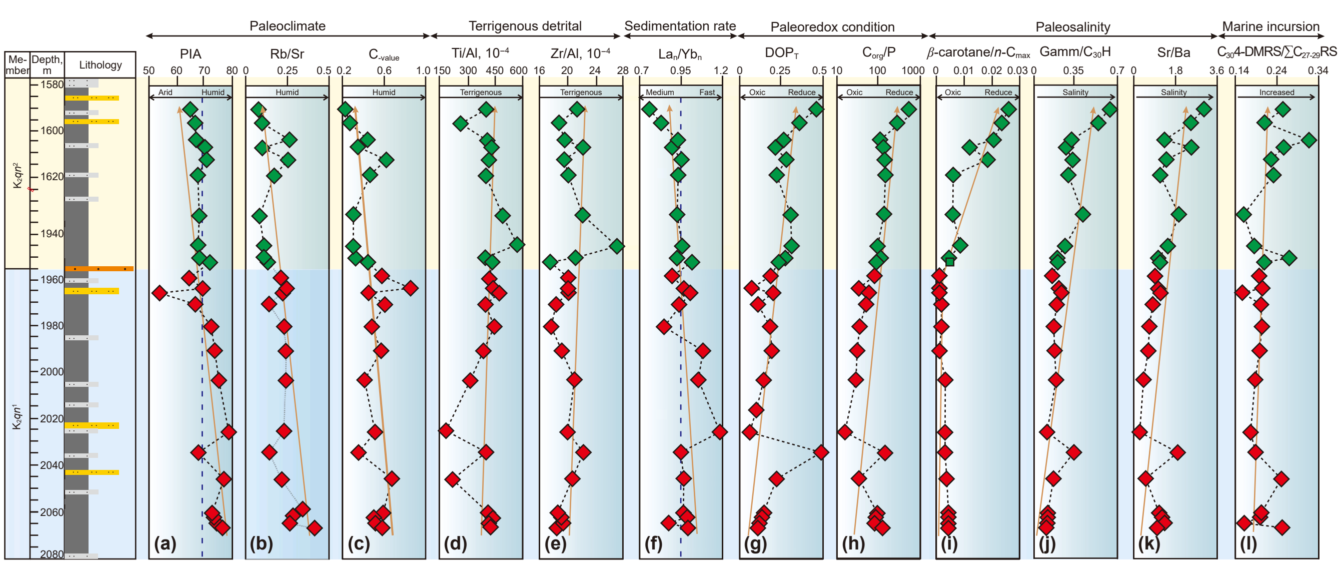

Fig. 8. Stratigraphic profiles of paleoclimate, terrigenous detrital influx, sedimentation rate, paleoredox condition, paleosalinity, and marine intrusion parameters.

stratification, and exacerbated benthic hypoxia (Chen et al., 2024; Zhu et al., 2017) as well as redox-driven phosphorus cycling (Figs. 8(h) and S3(d); Algeo and Ingall, 2007). In summary, convergent biomarker and inorganic geochemical proxies reveal a dynamic coupling between climate and lacustrine redox conditions, characterized by a progressive shift from oxic to suboxic

Petroleum Science 23 (2026) 3282–3298

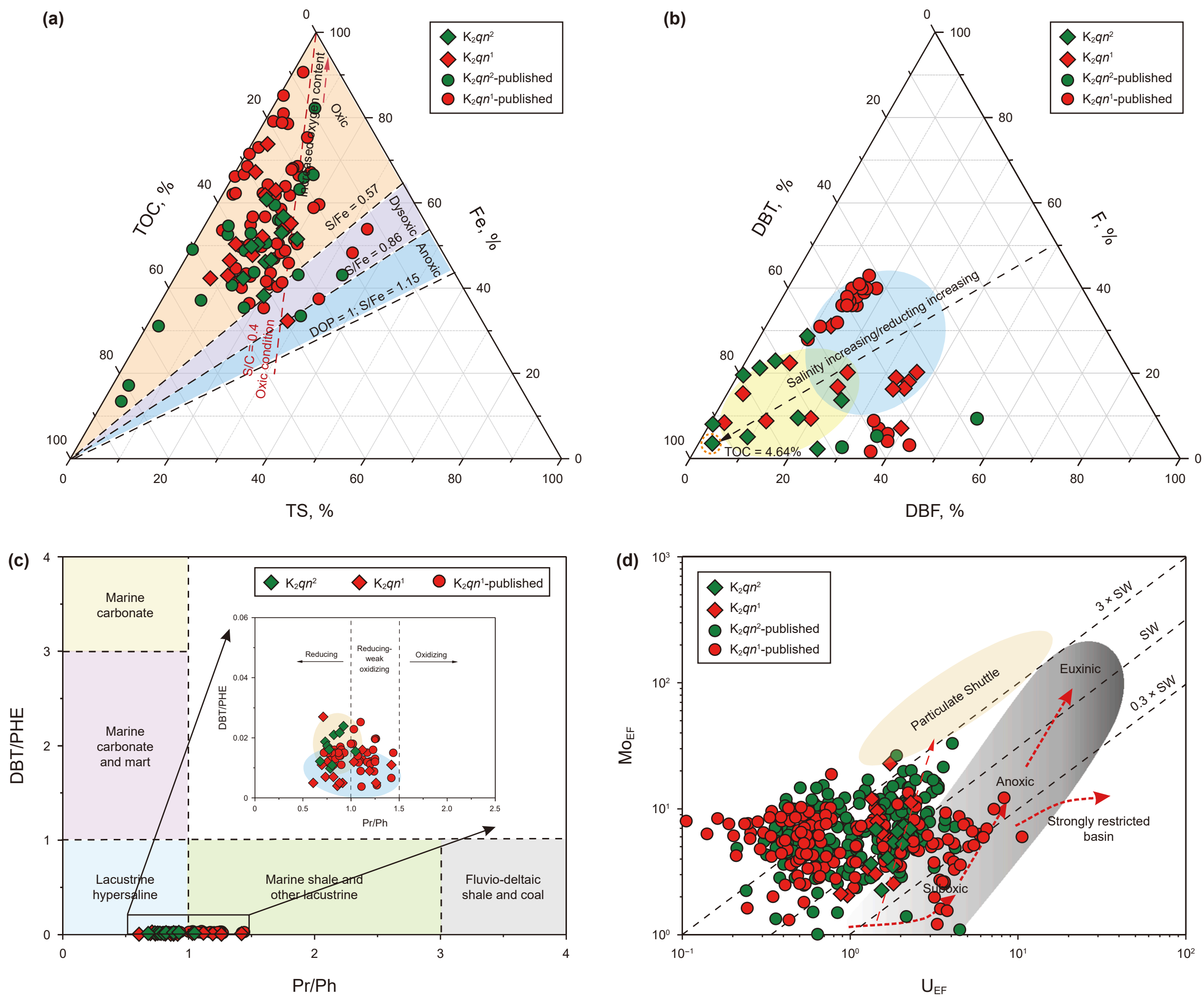

Fig. 9. Ternary diagrams of **(a)** TS, Fe, and TOC (Dean and Arthur, 1989), and **(b)** F, DBF, and DBT (after Qiao et al., 2024), as well as cross-plots of **(c)** Pr/Ph vs. DBT/PHE (Peters et al., 2005) and **(d)** U_{EF} vs. Mo_{EF} (Tribovillard et al., 2012), showing the paleoredox and paleosalinity conditions.

conditions during the K_2qn^1 interval toward sustained dysoxic to weakly anoxic conditions during the K_2qn^2 interval.

5.3.3. *Paleosalinity*

Salinity is a critical control on OM preservation, modulating microbial activity and redox gradients in lacustrine systems (Lu et al., 2025; Zheng et al., 2022b). Multiple proxies record a coherent increase in paleosalinity from the K_2qn^1 to the K_2qn^2 interval, consistent with climatic aridification.

The predominance of samples in the hypersaline field on a Pr/Ph vs. DBT/PHE cross-plot (Fig. 9(c)) indicates sulfate-limited conditions. Increasing DBT/PHE ratios and ternary partitioning of F, DBF, and DBT (Fig. 9(b)) from the K_2qn^1 to the K_2qn^2 intervals point to progressive salinization driven by reduced precipitation and enhanced evaporation. This is further supported by decreased MTTC ratios (Table S4) and elevated abundances of salinity-sensitive biomarkers, i.e., β-carotane (derived from halotolerant carotenoid-rich algae) and gammacerane. These ratios vary synchronously, demonstrating coupled climatic control on both salinity and water-column stratification (Figs. 8(i)–(j) and S3(c)).

Inorganic geochemical data reinforce this pattern. Sr/Ba ratios, interpreted using established thresholds (freshwater of <0.2; brackish of 0.2–0.5; saline of >0.5; Wei and Algeo, 2020), show a clear upsection increase after excluding samples with CaO >5% to avoid carbonate bias (Figs. 8(k) and S3(c)). This trend reflects climatically driven evaporative-precipitative imbalance and hydrological restructuring.

Although elevated Sr/Ba ratios could in principle indicate intermittent marine intrusions, consistent with some prior models for the Qingshankou Fm. (Chen et al., 2024; Xu et al., 2021), multiple lines of evidence argue against this mechanism as the primary control on recorded salinity fluctuations. First, molecular evidence reveals a decoupling between marine influence and salinity trends. While the presence of C_{30} 4-desmethylsteranes confirms occasional marine input (Hou et al., 2000; Peters et al., 2005), this biomarker shows no significant correlation with salinity proxies (Fig. 8(l)). Second, the sustained presence of prasinophyte algae in K_2qn^2 contradicts the community collapse expected from a sudden marine transgression, instead supporting a scenario of progressive lacustrine salinization (Fig. 3(e); Chen et al., 2024; Xu et al., 2021). Third, statistical analysis demonstrates that paleosalinity proxies (including expanded datasets of Gamm/C_{30}H and Sr/Ba; Fig. S3(c)) correlate strongly with paleoclimate indices rather than with marine incursion indicators (Fig. S6(b)). Although isotopic records (Sr, S, and N) suggest that marine incursion frequency decreased from K_2qn^1 to K_2qn^2 and

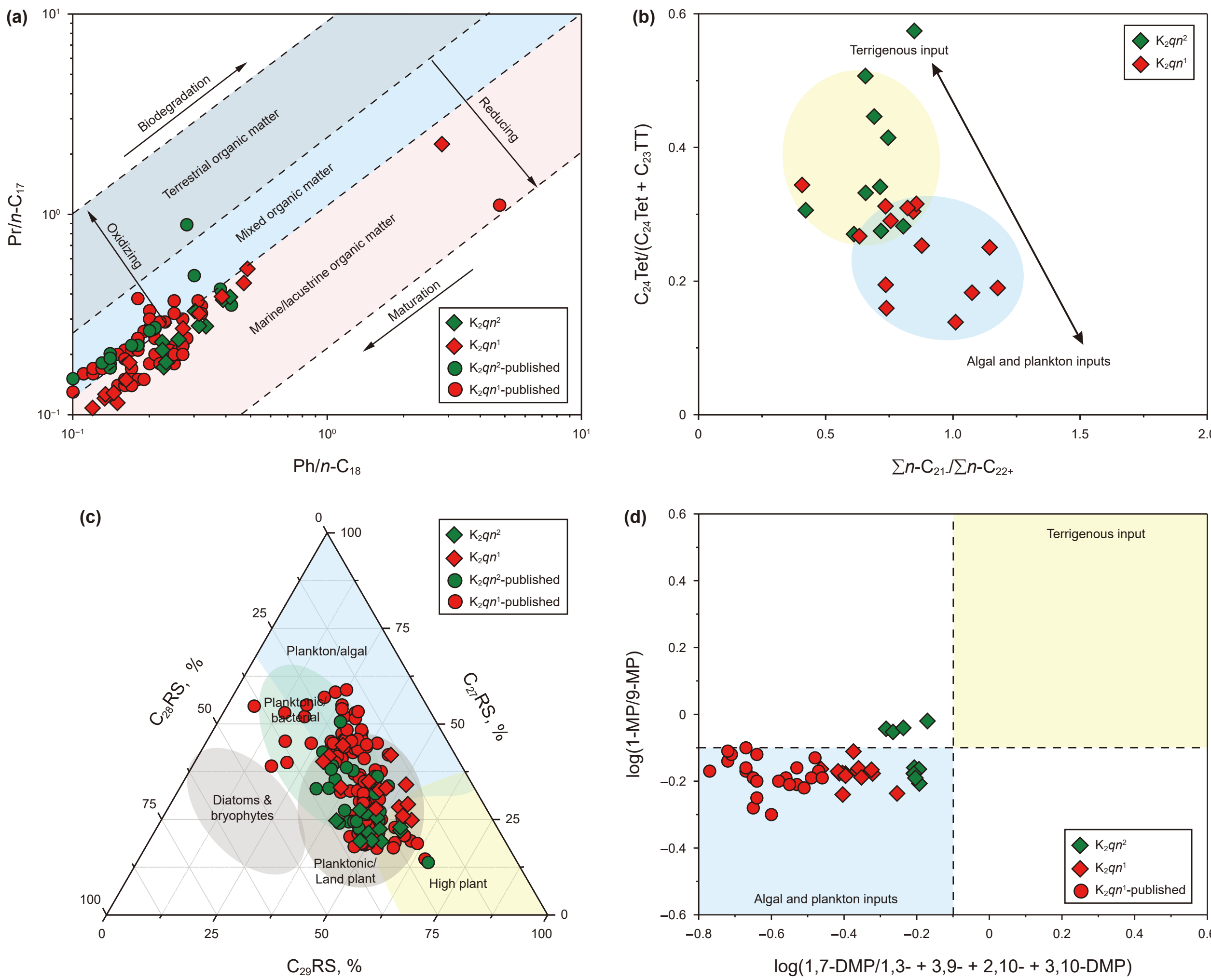

Fig. 10. Cross-plots of **(a)** Ph/n-C_{18} vs. Pr/n-C_{17} (Peters et al., 1999) and **(b)** $\sum n$-$C_{21-}/\sum n$-C_{22+} vs. C_{24}Tet/(C_{24}Tet + C_{23}TT) (Peters et al., 2005), **(c)** ternary plot of C_{27}-C_{28}-C_{29}RS (Huang and Meinschein, 1979), and **(d)** log (1-MP/9-MP) vs. log (1,7-DMP/1,3- + 3,9- + 2,10- + 3,10-DMP) (after Qiao et al. (2024)), showing the biological sources of OM of the Qingshankou Fm. source rock.

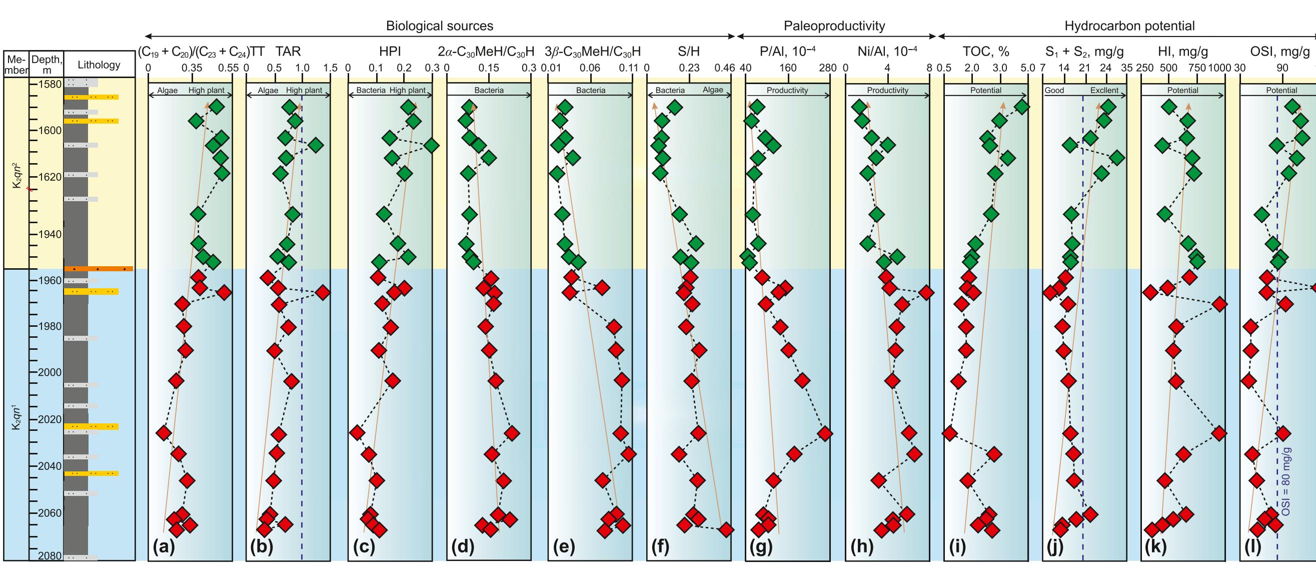

Fig. 11. Stratigraphic profiles of biological sources, paleoproductivity, and hydrocarbon potential parameters.

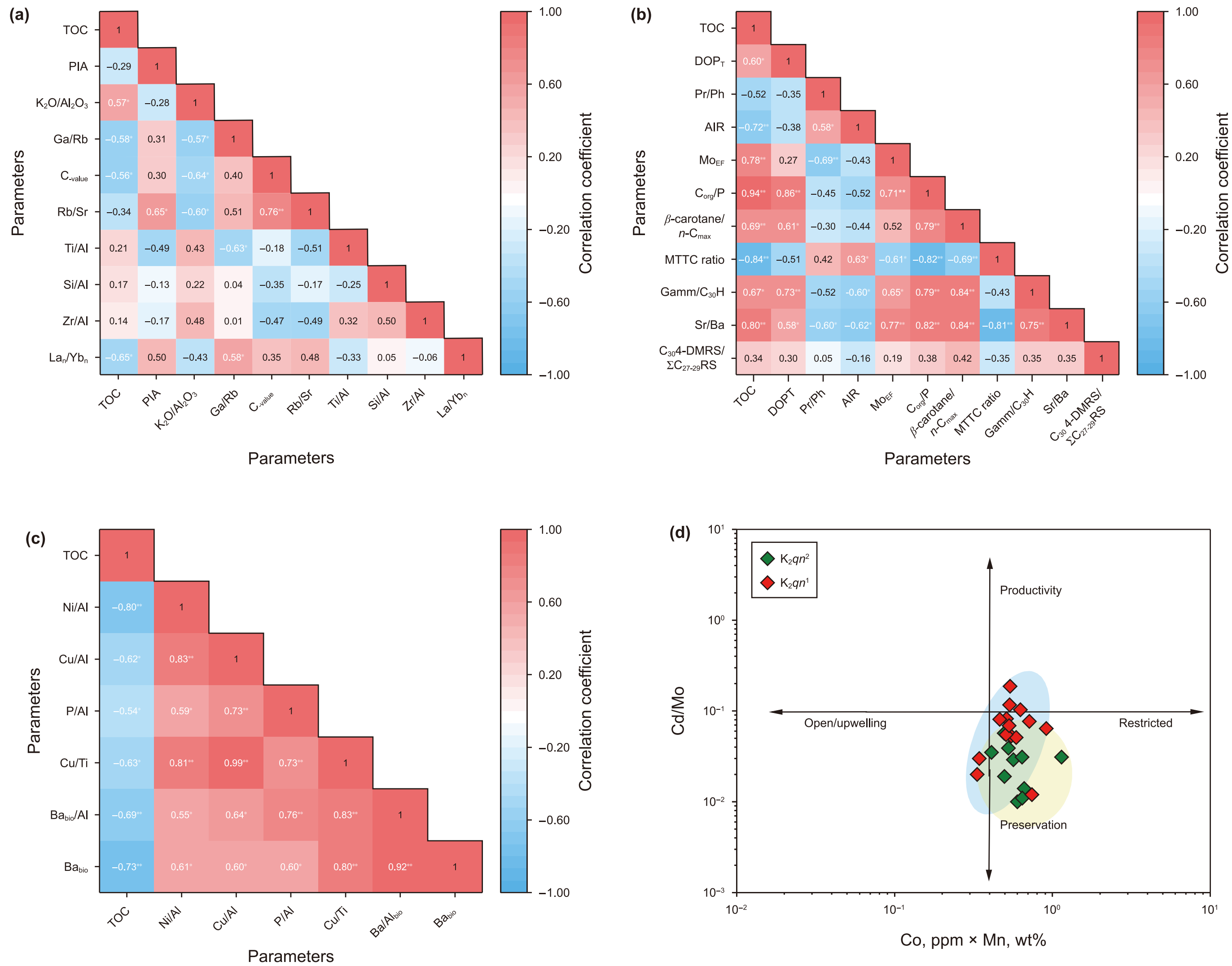

Fig. 12. The controlling factors of OM accumulation for the Qingshankou Fm. source rocks illustrated by **(a)** paleoclimate/weathering, detrital input, and sedimentation rate; **(b)** paleoredox, paleosalinity, and marine incursion; **(c)** paleoproductivity; and **(d)** the cross-plot of Co × Mn vs. Cd/Mo (Sweere et al., 2016).

covaried with sea-level (Chen et al., 2024; Tang et al., 2025; Zhu et al., 2023), their quantitative impact remains difficult to resolve due to spatial heterogeneity and unresolved incursion dynamics in the Central Depression. In summary, the convergent evidence indicates that long-term salinity evolution was dominantly controlled by climate-driven hydrology (i.e., the evaporation-precipitation balance), not by intermittent marine incursions.

5.4. Origin of organic matter

Petrographic analysis reveals that OM is dominated by lamalginite and mineral-bituminous matrix, with accessory vitrinite and inertinite (<10%; Fig. 3). This maceral assemblage indicates a primary aquatic biomass source, with limited terrestrial higher-plant input (Pickel et al., 2017).

Molecular evidence further constrains OM sources. The Ph/*n*-C_{18} vs. Pr/*n*-C_{17} cross-plot supports a dominant contribution from phytoplankton and benthic organisms (Fig. 10(a); Peters et al., 1999). *n*-Alkane distributions show that short-to mid-chain homologues (algae/aquatic macrophytes) prevail over long-chain components (terrestrial plant waxes) (Fig. 4(a) and (b)). Consistently, most samples exhibit $\sum n\text{-}C_{21-}/\sum n\text{-}C_{22+}$ ratios near 1, highlighting a strong aquatic signature that is especially pronounced in the K_2qn^1 interval (Fig. 10(b) and Supplementary Information 2). Temporal shifts in OM composition are evident across the climatic transition. Diagnostic tricyclic terpane ratios (C_{24}TeT/(C_{24}TeT + C_{23}TT) and (C_{19} + C_{20})/(C_{23} + C_{24})TT) increase markedly from the K_2qn^1 to K_2qn^2 intervals (Figs. 10(b) and 11(a)), indicating a relative decline in algal contribution under arid conditions (Peters et al., 2005; Volkman et al., 2015). Concurrently, prokaryotic inputs varied: monomethylalkanes (MMAs) attest to cyanobacterial contributions in both intervals (Fig. 4(a) and (b)), while specific archaeal and bacterial lipids (2*α*- and 3*β*-methylhopanes) point to additional microbial inputs, particularly from methanogens and halophilic archaea (Farrimond et al., 2004; Volkman et al., 2015; Zheng et al., 2022b). Although these compounds occur in trace amounts, their higher abundance in the K_2qn^1 interval suggests more active microbial communities under the preceding humid climate (Fig. S3(a)). While C_{27}, C_{28}, and C_{29} steranes are traditionally attributed to phytoplankton, diatoms, and higher plants, respectively (Huang and Meinschein, 1979), their sources in lacustrine settings are more complex. C_{29} steranes, in particular, can also derive from specific bacteria (e.g., cyanobacteria) and microalgae (Peters et al., 2005; Liu et al., 2023b; Wu et al., 2023). An integrated assessment of published data indicates that elevated C_{29}RS proportions in the studied formation primarily reflect algal-bacterial contributions, with a secondary input from terrestrial plants (Fig. 10(c)).

The 1,2,7-TMN is derived from oleanane-type triterpenoids, and 9-MP is primarily associated with algal-derived Type I/II kerogens. In contrast, 1,2,5-TMN, 1-MP, and 1,7-DMP originate from conifers (Strachan et al., 1988; Budzinski et al., 1995; Peters et al., 2005). In the studied samples, plots of log (1,2,7- + 1,6,7-TMN/1,3,7-TMN) versus log (1,2,5-TMN/1,3,6-TMN) (Fig. S3(b)) and of log (1-MP/9-MP) versus log (1,7-DMP/(1,3- + 3,9- + 2,10- + 3,10-DMP)) (Fig. 10(d)) consistently cluster within fields indicative of algal-dominated kerogens. These data, together with HPP values < 1 (Table S4), confirm a minor and stable contribution from higher plants.

Against this stable terrigenous background, pronounced shifts in aquatic OM are observed. The TAR increases markedly from the K_2qn^1 to K_2qn^2 intervals (Fig. 11(b)), reflecting a relative decline in algal-derived OM. This indicates suppressed primary productivity during the arid interval, likely due to climatic stressors such as reduced temperature and precipitation (Zheng et al., 2022a). Concurrently, bacterial contributions diminished under cooler conditions. The HPI increases inversely with paleotemperature proxies (Fig. 11(c)), signifying a relative decrease in bacterial input (Peters et al., 2005; Zheng et al., 2022b). This is corroborated by declining 2α-C_{30}MeH/C_{30}H and 3β-C_{30}MeH/C_{30}H ratios (Fig. 11(d) and (e)), which track cyanobacterial and proteobacterial communities (Farrimond et al., 2004). The reduction in these biomarkers can be directly attributed to climatic cooling, which inhibits microbial growth below species-specific thresholds (Peters et al., 2005; Wang et al., 2021). Notably, the sterane/hopane ratio (S/H) decreases more steeply across the transition than HPI and 2α-C_{30}MeH/C_{30}H from the K_2qn^1 to K_2qn^2 intervals (Fig. 11(f)). This steeper decline suggests that algal communities were more responsive to climate variability than bacterial populations, highlighting a differential response within the aquatic ecosystem (Zheng et al., 2022b).

In summary, the OM in the Qingshankou Fm. was predominantly derived from phytoplankton, aquatic algae, and bacteria, with stronger contributions during the relatively warm-humid K_2qn^1 interval than during the arid-cold K_2qn^2 interval. This contrast directly reflects the primary control exerted by paleoclimate on the lacustrine ecosystem, i.e., favorable conditions in the K_2qn^1 interval stimulated productivity, especially of climate-sensitive algae, whereas the shift to arid-cold regimes in the K_2qn^2 interval broadly suppressed biological proliferation.

5.5. Paleoproductivity and hydrocarbon potential

Primary productivity, a key control on OM accumulation, was reconstructed using multiple geochemical proxies. The Ba_{bio} content, which reflects phytoplankton assimilation and export (Schoepfer et al., 2015; Zheng et al., 2022a), is significantly higher in the humid K_2qn^1 than in the arid K_2qn^2 interval (Table S1). This trend is robustly supported by nutrient-element enrichment ratios (P/Al, Cu/Al, and Cu/Ti), proxies for biologically assimilated nutrients preserved with OM (Tribovillard et al., 2006), which are markedly elevated the K_2qn^1 interval (Fig. 11(g)). Parallel declines in Ba_{bio}/Al, Ni/Al (Fig. 11(h); Tables S1 and S5), and a synthesis of published data (Fig. S3(d)) confirm consistently higher productivity under humid conditions. Notably, the magnitude of key proxies is comparable to coeval Neo-Tethyan upwelling systems, indicating the Qingshankou paleolake sustained exceptionally high, marine-like productivity (Guo et al., 2024). These data, aligned with independent OM-source evidence, attest to prolific algal and bacterial biomass during the K_2qn^1 interval.

A striking paradox emerges: despite higher primary productivity and superior biomass quality in the K_2qn^1 interval, the K_2qn^2 interval exhibits systematically greater organic enrichment and higher shale-oil potential. This is evidenced by higher TOC, $S_1 + S_2$, EOM, HI, and oil saturation index (OSI) in the K_2qn^1 interval (Figs. 11(i)–(l) and S4(a)–(d)). Thermal maturity is ruled out as a driver, as T_{max} and R_o indicate comparable levels between intervals (Figs. 6, S4(e)–(f), and S5(a)–(b)), and restored TOC values match measurements closely (Niu et al., 2025). High S_1 and OSI values confirm effective in-situ hydrocarbon retention (Table S2; Lu et al., 2012).

The key to this paradox lies in the distinct depositional environments. While terrigenous input remained comparable, the K_2qn^1 interval was deposited under more oxygenated conditions, whereas the K_2qn^2 interval experienced more saline and reducing settings (Figs. 8 and 9). This climate-driven dichotomy fundamentally altered OM preservation and conversion efficiency. Hypersaline conditions in the K_2qn^2 interval promoted early hydrocarbon generation and higher conversion efficiency at a given thermal maturity (Feng et al., 2025), potentially aided by alkaline minerals prolonging lipid saponification (Cao et al., 2025). Consequently, a preservational-conversional divide emerged: oxygenated conditions during the K_2qn^1 interval limited OM preservation, whereas the saline, reducing conditions of the K_2qn^2 interval enhanced both, ultimately yielding higher shale-oil potential despite lower productivity.

5.6. Mechanisms and modes of organic matter accumulation

To unravel the controls on OM enrichment, systematic correlation analyses between TOC and 25 geochemical proxies were conducted (Fig. 12(a)–(c); Table S6). TOC shows only weak-to-moderate correlations with paleoclimate indices (e.g., PIA and Ga/Rb) and an extremely weak correlation with detrital input indicators, indicating neither climate nor terrigenous flux exerted a primary direct control.

Given comparable detrital flux, effective OM preservation in the more oxygenated K_2qn^1 interval would theoretically require low sedimentation rates. However, La_n/Yb_n values are markedly higher in most K_2qn^1 samples than in K_2qn^2 (Zhang et al., 2013; Figs. 7(f) and S3), indicating faster deposition. This is significant because TOC content typically increases with sedimentation rates up to a threshold (~5 cm/kyr), beyond which it declines due to OM dilution (Ding et al., 2015; Tyson, 2001), a pattern consistent with the lower TOC observed in the faster-deposited K_2qn^1 interval. Astrochronological constraints place sedimentation rates between 5.6 and 14.4 cm/kyr (Wu et al., 2013), within a range where increasing rate leads to OM dilution (Ding et al., 2015; Tyson, 2001). The significant negative correlation between TOC and sedimentation rate (Fig. 12(a)) supports dilution as a key constraint, consistent with the lower TOC observed in the faster-deposited K_2qn^1 interval.

Crucially, TOC exhibits strong positive correlations with redox and salinity proxies (e.g., Mo_{EF} and Sr/Ba; Fig. 12(b)), underscoring the dominance of preservation conditions. Elevated salinity enhanced water-column stratification, inhibited oxygen replenishment, and promoted benthic anoxia. These hypoxic conditions suppressed aerobic degradation, thereby facilitating net OM preservation (Algeo and Ingall, 2007; Lu et al., 2025). The case for a preservation-dominated regime is decisively strengthened by a clear paradox: key productivity proxies show significant negative correlations with TOC (Fig. 12(c)). This inverse relationship, corroborated by complementary redox-sensitive trace-metal

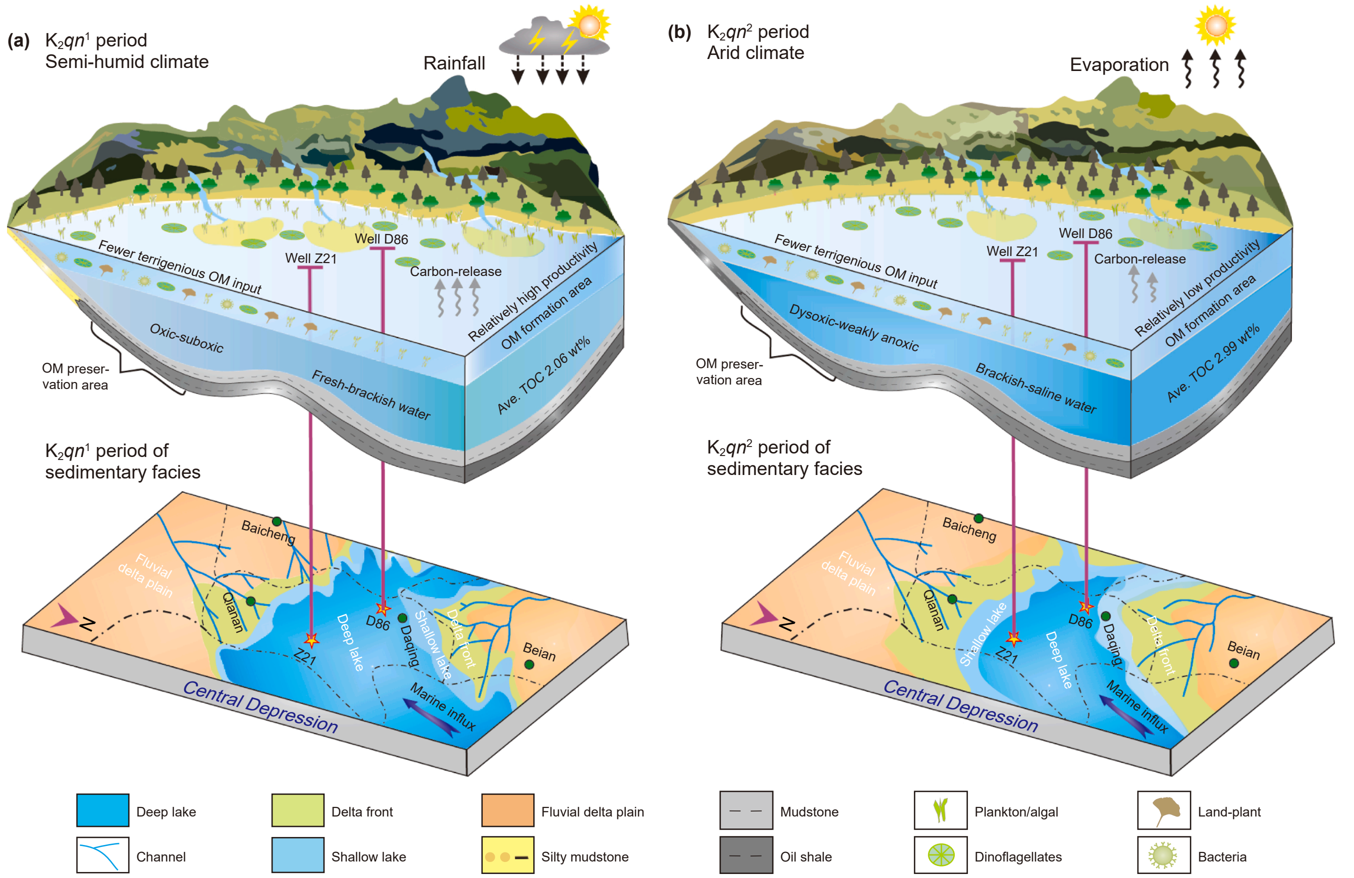

Fig. 13. The conceptual diagram illustrating distinct OM enrichment mechanisms in the lacustrine basin influenced by paleoclimate change during the **(a)** K_2qn^1 and **(b)** K_2qn^2 periods, respectively (modified from Zhang et al., 2022).

trends (e.g., Fig. 12(d)), demonstrates that higher productivity did not enhance burial and, in fact, coincided with lower enrichment.

Multivariate analyses clarify the paleoclimate's pivotal indirect role. Paleoclimate indices show strong correlations (up to 0.74) with key redox and salinity proxies (Fig. S6(a)), outlining a coherent climate-to-environment mechanism: aridification increased salinity via evaporative concentration, which enhanced water-column stratification and promoted benthic anoxia, thereby creating conditions conducive to OM preservation. Productivity proxies also correlate with climate indices (up to 0.83; Fig. S6(b)), confirming humid conditions stimulated algal-bacterial productivity. Thus, climate modulated both OM supply (productivity) and retention (preservation), with preservation being the dominant control on net accumulation.

Based on these findings, a climate-driven preservation model for differential OM enrichment in the Qingshankou Fm. is proposed. During the humid-warm K_2qn^1 interval, high productivity was offset by oxygenated waters and higher dilution rates, limiting net carbon burial (Fig. 13(a)). In contrast, aridification during the K_2qn^2 interval established a negative hydrological balance (evaporation > precipitation). Evaporative concentration increased salinity, strengthening stratification and creating a persistent "anoxic carbon trap" at the sediment-water interface. This dramatically enhanced OM preservation and hydrocarbon conversion efficiency, leading to greater carbon sequestration and shale-oil potential despite lower productivity (Fig. 13(b)). This fundamental shift from a productivity-driven to a preservation-dominated regime governed the lacustrine carbon cycle and ultimately determined the formation's hydrocarbon endowment.

6. Conclusions

This study deciphers the mechanistic links between Late Cretaceous climatic change and OM accumulation in the Qingshankou Fm. A major shift from humid (K_2qn^1 interval) to arid (K_2qn^2 interval) conditions fundamentally reorganized the lacustrine system, altering weathering, hydrology, and biotic productivity.

The humid K_2qn^1 interval climate sustained high primary productivity (e.g., from algae and cyanobacteria) but inhibited OM preservation due to a weakly stratified, more oxygenated water column. In contrast, aridification during the K_2qn^2 interval enhanced salinity stratification and benthic anoxia, dramatically improving preservation efficiency despite lower productivity. Thus, climate-mediated redox and salinity conditions rather than productivity exerted the dominant control on OM enrichment. This framework is statistically robust: preservation proxies correlate positively with aridity indices, while TOC content correlates inversely with productivity indicators. These results establish a clear climate-organic coupling that governed carbon burial, providing a predictive model for assessing hydrocarbon potential in analogous lacustrine systems.

CRediT authorship contribution statement

Zhao-Yang Wang: Writing – original draft, Methodology, Investigation, Formal analysis. **Jin-Qi Qiao:** Writing – review & editing, Supervision, Conceptualization, Funding acquisition. **Qing-Yong Luo:** Resources, Supervision, Validation, Writing –

review & editing. **Jia-Peng Wu:** Investigation, Data curation. **Man Lu:** Writing – review & editing. **Ye Zhang:** Resources. **Mikhail Spasennykh:** Writing – review & editing. **Hui-Long Lu:** Visualization, Formal analysis. **Lei He:** Visualization, Formal analysis.

Data availability

Data will be made available on request.

Declaration of competing interest

The authors declare that they have no conflicts of interest.

Acknowledgements

This study was granted financial support by the State Key Laboratory of Petroleum Resources and Engineering, China University of Petroleum (Beijing) (No. PRE/indep-2401). Thank all the team members of this paper for their hard work and teamwork.

Appendix A. Supplementary data

Supplementary data to this article can be found online at https://doi.org/10.1016/j.petsci.2026.01.027.

References

Algeo, T.J., Ingall, E., 2007. Sedimentary C_{org}:P ratios, paleocean ventilation, and Phanerozoic atmospheric pO_2. Palaeogeogr. Palaeoclimatol. Palaeoecol. 256, 130–155. https://doi.org/10.1016/j.palaeo.2007.02.029.
Algeo, T.J., Liu, J., 2020. A re-assessment of elemental proxies for paleoredox analysis. Chem. Geol. 540, 119545. https://doi.org/10.1016/j.chemgeo.2020.119549.
Budzinski, H., Garrigues, P., Connan, J., et al., 1995. Alkylated phenanthrene distributions as maturity and origin indicators in crude oils and rock extracts. Geochem. Cosmochim. Acta 59, 2043–2056. https://doi.org/10.1016/0016-7037(95)00125-5.
Cao, J., Zhang, R.J., Zhi, D.M., et al., 2025. Unique bimodal oil generation of alkaline-saline lacustrine source rock: evidences, model and mechanism of organic-inorganic interactions. Sci. China Earth Sci. 68, 1559–1582. https://doi.org/10.1007/s11430-024-1525-0.
Chen, R.Q., Bai, X., Huang, C.Z., et al., 2024. How marine incursions affect the sedimentary environment and the quality of source rocks in the Upper Cretaceous Songliao Basin, NE China. Mar. Petrol. Geol. 170, 107140. https://doi.org/10.1016/j.marpetgeo.2024.107140.
Cox, R., Lowe, D.R., Cullers, R.L., 1995. The influence of sediment recycling and basement composition on evolution of mudrock chemistry in the southwestern United States. Geochem. Cosmochim. Acta 59, 2919–2940. https://doi.org/10.1016/0016-7037(95)00185-9.
Dean, W., Arthur, M.A., 1989. Iron-sulfur-carbon relationships in organic carbon-rich sequences I: Cretaceous western interior sea way. Am. J. Sci. 289, 708–743. https://doi.org/10.2475/ajs.289.6.708.
Ding, X.J., Liu, G.D., Zha, M., et al., 2015. Relationship between total organic carbon content and sedimentation rate in ancient lacustrine sediments, a case study of Erlian basin, northern China. J. Geochem. Explor. 149, 22–29. https://doi.org/10.1016/j.gexplo.2014.11.004.
Farrimond, P., Talbot, H.M., Watson, D.F., et al., 2004. Methylhopanoids: Molecular indicators of ancient bacteria and a petroleum correlation tool. Geochem. Cosmochim. Acta 68, 3873–3882. https://doi.org/10.1016/j.gca.2004.04.011.
Fedo, C.M., Wayne Nesbitt, H., Young, G.M., 1995. Unraveling the effects of potassium metasomatism in sedimentary rocks and paleosols, with implications for paleoweathering conditions and provenance. Geology 23, 921–924. https://doi.org/10.1130/0091-7613(1995)023<0921:UTEOPM>2.3.CO;2.
Feng, D.H., Liu, C.L., Yang, X.Y., et al., 2025. Pyrolysis product characteristics and hydrocarbon generation-retention-expulsion model of alkaline lacustrine organic-rich shale. Fuel 395, 135239. https://doi.org/10.1016/j.fuel.2025.135239.
Feng, Z.Q., Jia, C.Z., Xie, X.N., et al., 2010. Tectonostratigraphic units and stratigraphic sequences of the nonmarine Songliao basin, northeast China. Basin Res. 22, 79–95. https://doi.org/10.1111/j.1365-2117.2009.00445.x.
Floyd, P.A., Leveridge, B.E., 1987. Tectonic environment of the Devonian Gramscatho basin, South Cornwall: Framework mode and geochemical evidence from turbiditic sandstones. J. Geol. Soc. 144, 531–542. https://doi.org/10.1144/gsjgs.144.4.0531.
Friedrich, O., Norris, R.D., Erbacher, J., 2012. Evolution of middle to Late Cretaceous oceans–A 55 my record of Earth's temperature and carbon cycle. Geology 40, 107–110. https://doi.org/10.1130/G327011.
Fryklund, B., Stark, P., 2020. Super basins—New paradigm for oil and gas supply. AAPG Bull. 104, 2507–2519. https://doi.org/10.1306/09182017314.
Garzanti, E., Padoan, M., Setti, M., et al., 2013. Weathering geochemistry and Sr-Nd fingerprints of equatorial upper Nile and Congo muds. Geochem. Geophys. Geosyst. 14, 292–316. https://doi.org/10.1002/ggge.20060.
Guo, H.F., Chen, X., Yao, H.W., et al., 2024. Quantifying the pattern of organic carbon burial through Cretaceous Oceanic Anoxic Event 2. Earth Sci. Rev. 257, 104903. https://doi.org/10.1016/j.earscirev.2024.104903.
Heathcote, A.J., Anderson, N.J., Prairie, Y.T., et al., 2015. Large increases in carbon burial in northern lakes during the Anthropocene. Nat. Commun. 6, 10016. https://doi.org/10.1038/ncomms10016.
Hou, D.J., Li, M.W., Huang, Q.H., 2000. Marine transgressional events in the gigantic freshwater lake Songliao: Paleontological and geochemical evidence. Org. Geochem. 31, 763–768. https://doi.org/10.1016/S0146-6380(00)00065-6.
Huang, W.Y., Meinschein, W.G., 1979. Sterols as ecological indicators. Geochem. Cosmochim. Acta 43, 739–745. https://doi.org/10.1016/0016-7037(79)90257-6.
Jones, M.M., Ibarra, D.E., Gao, Y., et al., 2018. Evaluating Late Cretaceous OAEs and the influence of marine incursions on organic carbon burial in an expansive East Asian paleo-lake. Earth Planet Sci. Lett. 484, 41–52. https://doi.org/10.1016/j.epsl.2017.11.046.
Kang, Y., Liu, K.Q., Zhu, R.K., et al., 2024. The evolution of clay mineral and its indication of hydrocarbons under overpressure: An example from the shale of the Qingshankou formation in the Gulong Sag. Pet. Sci. 21, 3867–3883. https://doi.org/10.1016/j.petsci.2024.07.007.
Lei, Y., Cao, H.R., Wang, X.Y., et al., 2022. Polycyclic aromatic hydrocarbons in the Upper Cretaceous lacustrine deposits from the Songliao Basin (NE China): Implications for wildfires and paleoclimate. Palaeogeogr. Palaeoclimatol. Palaeoecol. 600, 111083. https://doi.org/10.1016/j.palaeo.2022.111083.
Li, L., Bao, Z.D., Li, L., et al., 2024. The source and preservation of lacustrine shale organic matter: Insights from the Qingshankou Formation in the Changling Sag, Southern Songliao Basin, China. Sediment. Geol. 466, 106649. https://doi.org/10.1016/j.sedgeo.2024.106649.
Li, X., Huang, Y.J., Zhang, Z.F., et al., 2022. Chemical weathering characteristics of the Late Cretaceous Nenjiang Formation from the Songliao Basin (Northeastern China) reveal prominent Milankovitch band variations. Palaeogeogr. Palaeoclimatol. Palaeoecol. 601, 111130. https://doi.org/10.1016/j.palaeo.2022.111130.
Li, Z.Y., Zhang, Y.G., Torres, M., et al., 2023. Neogene burial of organic carbon in the global ocean. Nature 613, 90–95. https://doi.org/10.1038/s41586-022-05413-6.
Liu, B., Liu, L.B., Fu, J., et al., 2023a. The songliao super Basin in northeastern China. AAPG Bull. 107, 1257–1297. https://doi.org/10.1306/02242321181.
Liu, D.D., Fan, Q.Q., Zhang, C., et al., 2022. Paleoenvironment evolution of the Permian Lucaogou Formation in the southern Junggar Basin, NW China. Palaeogeogr. Palaeoclimatol. Palaeoecol. 603, 111198. https://doi.org/10.1016/j.palaeo.2022.111198.
Liu, S.J., Gao, G., Gang, W.Z., et al., 2023b. Differences in geochemistry and hydrocarbon generation of source-rock samples dominated by telalginite and lamalginite: A case study on the Permian saline lacustrine source rocks in the Jimusaer Sag, NW China. Pet. Sci. 20, 141–160. https://doi.org/10.1016/j.petsci.2022.08.034.
Lu, M., Duan, G.Q., Zhang, T.X., et al., 2025. Influences of paleoclimatic changes on organic matter enrichment mechanisms in freshwater and saline lacustrine oil shales in China: A machine learning approach. Earth Sci. Rev. 262, 105061. https://doi.org/10.1016/j.earscirev.2025.105061.
Lu, S.F., Huang, W.B., Chen, F.W., et al., 2012. Classification and evaluation criteria of shale oil and gas resources: Discussion and application. Petrol. Explor. Dev. 39, 268–276. https://doi.org/10.1016/s1876-3804(12)60042-1.
McLennan, S.M., 1989. Rare earth elements in sedimentary rocks: Influence of provenance and sedimentary process. In: Lipin, B.R., McKay, G.A. (Eds.), Geochemistry and Mineralogy of Rare Earth Elements, vol. 21. Rev. Mineral., pp. 169–200. https://doi.org/10.1515/9781501509032-010
Niu, D.M., Li, T.Y., Bai, Y.Y., et al., 2025. Restoring the original hydrocarbon-generating potential of deep source rocks: A critical review and a novel method using the Songliao Basin, China, as a case study. Int. J. Coal Geol. 303, 104741. https://doi.org/10.1016/j.coal.2025.104741.
Peters, K.E., Fraser, T.H., Amris, W., et al., 1999. Geochemistry of crude oils from eastern Indonesia. AAPG Bull. 83, 1927–1942. https://doi.org/10.1306/E4FD4643-1732-11D7-8645000102C1865D.
Peters, K.E., Walters, C.C., Moldowan, J.M., 2005. The Biomarker Guide. Biomarkers and Isotopes in the Petroleum Exploration and Earth History, second ed. Cambridge University Press, New York.
Pickel, W., Kus, J., Flores, D., et al., 2017. Classification of liptinite–ICCP System 1994. Int. J. Coal Geol. 169, 40–61. https://doi.org/10.1016/j.coal.2016.11.004.
Qiao, J.Q, Littke, R., Grohmann, S., et al., 2022. Climatic and environmental conditions during the Pleistocene in the Central Qaidam Basin, NE Tibetan Plateau: Evidence from GDGTs, stable isotopes and major and trace elements of the Qigequan Formation. Int. J. Coal Geol. 254, 103958. https://doi.org/10.1016/j.coal.2022.103958.
Qiao, J.Q., Luo, Q.Y., Guo, S.X., et al., 2024. Organic petrology and geochemistry of the late Neogene Shizigou Formation in the Qaidam Basin, China: Characteristics of a prospective microbial gas source rock. Int. J. Coal Geol. 296, 104658. https://doi.org/10.1016/j.coal.2024.104658.

Qiao, J.Q., Luo, Q.Y., Tang, X.L., et al., 2025. Geochemistry and mineralogy of the late Neogene alkaline megalake sediments in the Qaidam Basin (China): Implications for provenance, tectonics, paleoclimate, paleoenvironment and organic matter accumulation. Appl. Geochem. 183, 106339. https://doi.org/10.1016/j.apgeochem.2025.106339.
Qiao, J.Q., Luo, Q.Y., Zhang, K.H., et al., 2023. Geochemistry and organic petrography of the Middle Permian Lucaogou alkaline lacustrine oil shale in the southern Junggar Basin, China: Implications for formation conditions and organic matter accumulation. Int. J. Coal Geol. 268, 104198. https://doi.org/10.1016/j.coal.2023.104198.
Roy, D.K., Roser, B.P., 2013. Climatic control on the composition of Carboniferous–Permian Gondwana sediments, Khalaspir basin, Bangladesh. Gondwana Res. 23, 1163–1171. https://doi.org/10.1016/j.gr.2012.07.006.
Schoepfer, S.D., Shen, J., Wei, H.Y., et al., 2015. Total organic carbon, organic phosphorus, and biogenic barium fluxes as proxies for paleomarine productivity. Earth Sci. Rev. 149, 23–52. https://doi.org/10.1016/j.earscirev.2014.08.017.
Scotese, C.R., Song, H., Mills, B.J.W., et al., 2021. Phanerozoic paleotemperatures: The Earth's changing climate during the last 540 million years. Earth Sci. Rev. 215, 103503. https://doi.org/10.1016/j.earscirev.2021.103503.
Seifert, W.K., Michael Moldowan, J., 1978. Applications of steranes, terpanes and monoaromatics to the maturation, migration and source of crude oils. Geochem. Cosmochim. Acta 42, 77–95. https://doi.org/10.1016/0016-7037(78)90219-3.
Strachan, M.G., Alexander, R., Kagi, R.I., 1988. Trimethylnaphthalenes in crude oils and sediments: Effects of source and maturity. Geochem. Cosmochim. Acta 52, 1255–1264. https://doi.org/10.1016/0016-7037(88)90279-7.
Sun, N.L., Zhang, J.Y., Zhong, J.H., et al., 2025. Sedimentary processes of fine-grained sedimentary rocks in lacustrine basins: A case study of the Upper Cretaceous Qingshankou Formation, northern Songliao Basin, China. Sediment. Geol. 490, 106987. https://doi.org/10.1016/j.sedgeo.2025.106987.
Suttner, L.J., Dutta, P.K., 1986. Alluvial sandstone composition and paleoclimate; I, Framework mineralogy. J. Sediment. Res. 56, 329–345. https://doi.org/10.1306/212F8909-2B24-11D7-8648000102C1865D.
Sweere, T., van den Boorn, S., Dickson, A.J., et al., 2016. Definition of new trace-metal proxies for the controls on organic matter enrichment in marine sediments based on Mn, Co, Mo and Cd concentrations. Chem. Geol. 441, 235–245. https://doi.org/10.1016/j.chemgeo.2016.08.028.
Tang, B.Q., Meng, Q.T., Hu, F., et al., 2025. Orbital forcing on lacustrine shale deposition in the Late Cretaceous Songliao Basin, Northeastern China: Responses and synergistic effects of organic matter sources, paleoenvironment, and seawater incursion events. Palaeogeogr. Palaeoclimatol. Palaeoecol. 676, 113133. https://doi.org/10.1016/j.palaeo.2025.113133.
Tribovillard, N., Algeo, T.J., Baudin, F., et al., 2012. Analysis of marine environmental conditions based on molybdenum uranium covariation-Applications to Mesozoic paleoceanography. Chem. Geol. 324–325, 46–58. https://doi.org/10.1016/j.chemgeo.2011.09.009.
Tribovillard, N., Algeo, T.J., Lyons, T., et al., 2006. Trace metals as paleoredox and paleoproductivity proxies: An update. Chem. Geol. 232, 12–32. https://doi.org/10.1016/j.chemgeo.2006.02.012.
Tyson, R.V., 2001. Sedimentation rate, dilution, preservation and total organic carbon: Some results of a modelling study. Org. Geochem. 32, 333–339. https://doi.org/10.1016/S0146-6380(00)00161-3.
Volkman, J.K., Zhang, Z., Xie, X., et al., 2015. Biomarker evidence for Botryococcus and a methane cycle in the Eocene Huadian oil shale, NE China. Org. Geochem. 78, 121–134. https://doi.org/10.1016/j.orggeochem.2014.11.002.
Wang, T.T., Ramezani, J., Wang, C.S., et al., 2016. High-precision U-Pb geochronologic constraints on the Late Cretaceous terrestrial cyclostratigraphy and geomagnetic polarity from the Songliao Basin, Northeast China. Earth Planet Sci. Lett. 446, 37–44. https://doi.org/10.1016/j.epsl.2016.04.007.
Wang, X.L., Algeo, T.J., Li, C., et al., 2023a. Spatial pattern of marine oxygenation set by tectonic and ecological drivers over the Phanerozoic. Nat. Geosci. 16, 1020–1026. https://doi.org/10.1038/s41561-023-01296-y.
Wang, X.L., Zhu, X.M., Lai, J., et al., 2024. Paleoenvironmental reconstruction and organic matter accumulation of the paleogene shahejie oil shale in the Zhanhua Sag, Bohai Bay Basin, Eastern China. Pet. Sci. 21, 1552–1568. https://doi.org/10.1016/j.petsci.2024.03.001.
Wang, Y.C., Li, P.P., Feng, Z.H., et al., 2023b. Geochemical characteristics of shales from the first member of Qingshankou Formation in Gulong Sag, Songliao Basin, China: Implication for mechanism of organic matter enrichment. Mar. Petrol. Geol. 150, 106142. https://doi.org/10.1016/j.marpetgeo.2023.106142.
Wang, Z., Tsementzi, D., Williams, T.C., et al., 2021. Environmental stability impacts the differential sensitivity of marine microbiomes to increases in temperature and acidity. ISME J. 15, 19–28. https://doi.org/10.1038/s41396-020-00748-2.
Wei, W., Algeo, T.J., 2020. Elemental proxies for paleosalinity analysis of ancient shales and mudrocks. Geochem. Cosmochim. Acta 287, 341–366. https://doi.org/10.1016/j.gca.2019.06.034.
Wu, H.C., Zhang, S.H., Jiang, G.Q., et al., 2013. Astrochronology of the Early Turonian–Early Campanian terrestrial succession in the Songliao Basin, northeastern China and its implication for long-period behavior of the Solar system. Palaeogeogr. Palaeoclimatol. Palaeoecol. 385, 55–70. https://doi.org/10.1016/j.palaeo.2012.09.004.
Wu, Z.R., Littke, R., Baniasad, A., et al., 2023. Geochemistry and petrology of petroleum source rocks in the Upper Cretaceous Qingshankou Formation, Songliao Basin, NE China. Int. J. Coal Geol. 270, 104222. https://doi.org/10.1016/j.coal.2023.104222.
Xu, C., Shan, X.L., He, W.T., et al., 2021. The influence of paleoclimate and a marine transgression event on organic matter accumulation in lacustrine black shales from the Late Cretaceous, southern Songliao Basin, Northeast China. Int. J. Coal Geol. 246, 103842. https://doi.org/10.1016/j.coal.2021.103842.
Xu, J.J., Liu, Z.J., Bechtel, A., et al., 2019. Organic matter accumulation in the Upper Cretaceous Qingshankou and Nenjiang formations, Songliao Basin (NE China): Implications from high-resolution geochemical analysis. Mar. Petrol. Geol. 102, 187–201. https://doi.org/10.1016/j.marpetgeo.2018.12.037.
Zhang, M.M, Liu, Z.J, Xu, S.C, et al., 2013. Element response to the ancient lake information and its evolution history of argillaceous source rocks in the Lucaogou Formation in Sangonghe area of southern margin of Junggar Basin. J. Earth Sci. 24, 987–996. https://doi.org/10.1007/s12583-013-0392-4.
Zhang, P.L., Misch, D., Meng, Q.T., et al., 2022. Lateral changes of organic matter preservation in the lacustrine Qingshankou Formation (Cretaceous Songliao Basin, NE China): Evidence for basin segmentation. Int. J. Coal Geol. 254, 103984. https://doi.org/10.1016/j.coal.2022.10398.
Zhang, S.C., Wang, H.J., Liu, Y.K., et al., 2024. Lacustrine carbon sink: A hidden driver of the Late Cretaceous Cooling Event. Sci. Bull. 69, 3949–3958. https://doi.org/10.1016/j.scib.2024.06.024.
Zhao, J., Wan, X.Q., Xi, D.P., et al., 2014. Late Cretaceous palynology and paleoclimate change: Evidence from the SK1 (south) core, Songliao Basin, NE China. Sci. China Earth Sci. 57, 2985–2997. https://doi.org/10.1007/s11430-014-4975-4.
Zheng, R.H., Zeng, W.R., Li, Z.P., et al., 2022a. Differential enrichment mechanisms of organic matter in the Chang 7 Member mudstone and shale in Ordos Basin, China: Constraints from organic geochemistry and element geochemistry. Palaeogeogr. Palaeoclimatol. Palaeoecol. 601, 111126. https://doi.org/10.1016/j.palaeo.2022.111126.
Zheng, T.Y., Zieger, L., Baniasad, A., et al., 2022b. The Shahejie Formation in the Dongpu Depression, Bohai Bay Basin, China: Geochemical investigation of the origin, deposition and preservation of organic matter in a saline lacustrine environment during the Middle Eocene. Int. J. Coal Geol. 253, 103967. https://doi.org/10.1016/j.coal.2022.103967.
Zhu, X.M., Cao, J., Xia, L.W., et al., 2023. Links between marine incursions, lacustrine anoxia and organic matter enrichment in the Upper Cretaceous Qingshankou Formation, Songliao Basin, China. Mar. Petrol. Geol. 158, 106535. https://doi.org/10.1016/j.marpetgeo.2023.106536.
Zhu, X.M., Zeng, H.L., Li, S.L., et al., 2017. Sedimentary characteristics and seismic geomorphologic responses of a shallow-water delta in the Qingshankou Formation from the Songliao Basin, China. Mar. Petrol. Geol. 79, 131–148. https://doi.org/10.1016/j.marpetgeo.2016.09.018.
Zou, C.N., Zhu, R.K., Chen, Z.Q., et al., 2019. Organic-matter-rich shales of China. Earth Sci. Rev. 189, 51–78. https://doi.org/10.1016/j.earscirev.2018.12.002.